Chapter 4

Dielectric Properties of Pristine and Modified C_{60} Films

4.1 Introduction

Since the discovery by Krätschmer *et al.* [7] of the method for bulk synthesis of fullerene C_{60} (see Section 1.2), the complex dielectric function $\varepsilon(\omega) = \varepsilon'(\omega) - j\varepsilon''(\omega)$ of solid C_{60} films has been studied over a broad frequency range using a wide variety of techniques [24, 25, 45, 61, 76, 234].

In this chapter, we present the results of our studies of the C_{60} dielectric function $\varepsilon(\omega)$ at the low end of the frequency spectrum (0.01 Hz–100 kHz). We shall start, however, by giving an overview of $\varepsilon(\omega)$ at optical frequencies (Sec. 4.2). Experimental difficulties in obtaining intrinsic properties of C_{60}-based solids are discussed in Sec. 4.3. In Sec. 4.4, we explain the motivation underlying the efforts to improve the dielectric properties of C_{60} films by intercalation of various foreign species into the interstitial spaces of the solid. The justification for molecular oxygen intercalation is given in Sec. 4.4.1, and the feasibility of using other gases (Cl_2, NO) as intercalants is discussed. Sec. 4.5 is devoted to techniques of fullerene thin film sample preparation and characterization. The results of the measurements of $\varepsilon(\omega)$ as a function of impurity diffusion and as a function of temperature are presented in Sections 4.7 and 4.8, respectively.

4.2 Optical dielectric function of C_{60}

The optical dielectric function $\varepsilon(\omega)$ of C_{60} has been mapped out in the range of 10^{13}–10^{16} Hz (corresponding to 0.05–40 eV) using infrared, vis-UV, and electron energy loss spectroscopies. Figure 4-1 presents a summary of experimental data reported for the real $\varepsilon'(\omega)$ and imaginary $\varepsilon''(\omega)$ parts of the dielectric function at 300 K over the entire optical frequency range from the infrared through the ultraviolet.

In Fig. 4-1, the features in the optical dielectric function below ~0.3 eV are due to molecular vibrations (see Sec. 1.6), and can be associated with the four strong first-order F_{1u} intramolecular modes (at 526, 576, 1183, and 1428 cm^{-1}, as detailed in Table 1.3) and two strong combination $(\omega_1+\omega_2)$ modes (at 1539 cm^{-1} and 2328 cm^{-1}) first observed by Krätschmer *et al.* [7] from measurements of the infrared absorption spectrum of a C_{60} film. Transmission experiments carried out on thicker (~2-3 μm) films reveal numerous (~100) additional features attributed to other intramolecular combination modes [108], which also enter into $\varepsilon(\omega)$. The IR peaks in Fig. 4-1 have been successfully fit [235] to the standard Drude-Lorentz model [236], in which the complex dielectric function $\varepsilon(\omega)$ is given by the sum of contributions from a background core real constant ε_∞, a Drude (or free carrier) term $\varepsilon_{\text{Drude}}(\omega)$ and a phonon term $\varepsilon_{\text{phonon}}(\omega)$ [235].

$$\varepsilon(\omega) = \varepsilon'(\omega) - j\varepsilon''(\omega) = \varepsilon_\infty + \varepsilon_{\text{Drude}}(\omega) + \varepsilon_{\text{phonon}}(\omega) \tag{4.1}$$

where

$$\varepsilon_{\text{Drude}}(\omega) = \frac{-\omega_p^2}{\omega(\omega - j/\tau)} \tag{4.2}$$

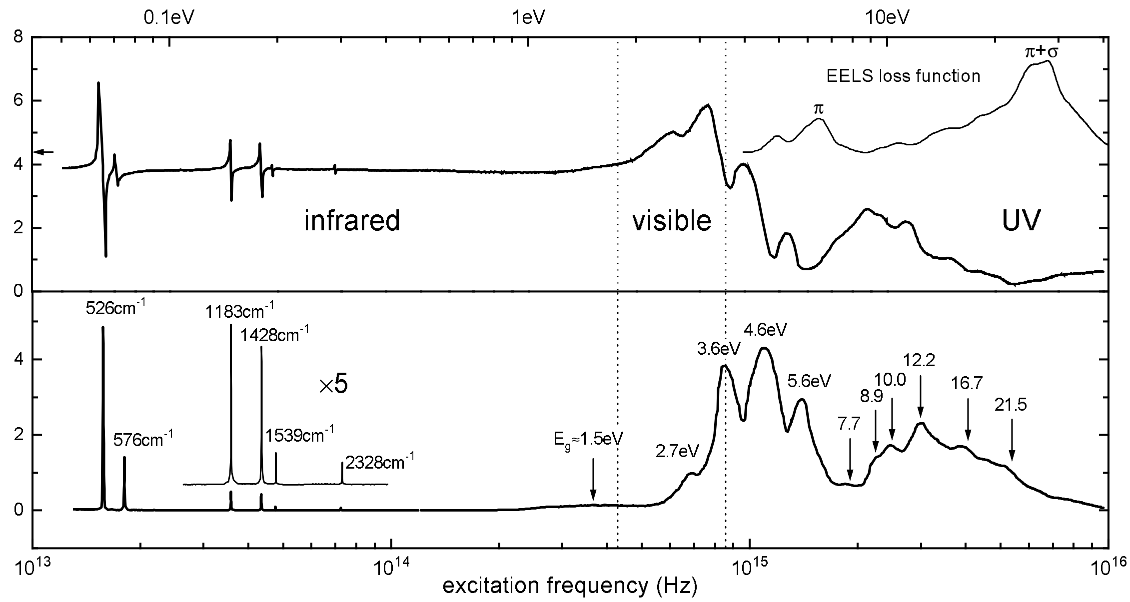

Figure 4-1: Summary of real $\varepsilon'(\omega)$ and imaginary $\varepsilon''(\omega)$ parts of the dielectric function for C_{60} vacuum-sublimed solid films at room temperature over all optical frequencies. The data between 0.05 and 0.5 eV (mid- to near-infrared) were collected using the Fourier transform infrared (FTIR) transmission technique [45]. The vis-UV range was investigated by variable angle spectroscopic ellipsometry (VASE) [25] and near-normal-incidence reflection and transmission experiments [61]. UV data above ~7 eV were obtained using electron energy loss spectroscopy (EELS) [234] by Kramers-Kronig analysis of the EELS loss function (inset). The arrow at the left axis points to $\varepsilon' = 4.4$, the observed low frequency value of the dielectric constant [24].

and

$$\varepsilon_{\text{phonon}}(\omega) = \sum_{i=1}^{n} \frac{f_i \omega_i^2}{\omega_i^2 - \omega^2 + j\Gamma_i \omega}. \tag{4.3}$$

In the Drude term, ω_p is the free carrier plasma frequency and τ is the free carrier scattering time. For the i^{th} phonon contribution, f_i, ω_i and Γ_i are the oscillator strength, frequency and damping, respectively, for each IR mode (see Ref. [235] for a listing of oscillator parameters).

As the absorption edge of C_{60} solid has been determined to be ~1.5 eV [85], the structure in $\varepsilon(\omega)$ in the visible-UV range below ~7 eV (see Fig. 4-1) is primarily of electronic origin, and may be assigned to electronic transitions between carbon π (bonding) and π^* (antibonding) electron states (Sec. 1.4). The data in this range were obtained by Ren *et al.* [25] for films vacuum deposited on Si(100) using variable angle spectroscopic ellipsometry (VASE), and by Wang *et al.* [61] on films deposited on quartz (Suprasil) from near-normal-incidence reflection and transmission experiments. The four broad peaks in this range (at 2.7, 3.6, 4.6, and 5.6 eV [25, 61]) are identified with dipole-allowed electronic transitions, and can also be described by a sum of Lorentz oscillators (see Ren *et al.* [25], Wang *et al.* [61], and Kelly *et al.* [237] for a table of oscillator parameters). In this case, each oscillator function corresponds to a transition between narrow electronic energy bands derived from C_{60} molecular orbitals. The core dielectric constant ε_∞, used to approximate interband absorption well beyond the range of the data [61], has been found to equal $\varepsilon_\infty \approx 2.4$ [25, 61]. The success of the Lorentz oscillator fits at both infrared and vis-UV frequencies corroborates the strong molecular character of the C_{60} solid (Sec. 1.3.2).

To obtain the dielectric function $\varepsilon(\omega)$ in the UV range above ~7 eV not easily accessible by optical techniques, the electron energy loss spectroscopy (EELS) has been successfully employed [234, 238]. In the inset to Fig. 4-1, the two dominant peaks in the frequency dependence of the EELS loss function $\mathcal{I}m\{-1/\varepsilon(\omega)\}$ for small momentum transfer ($q = 0.1$ Å^{-1}) occur at ~6 eV for the π-plasmon and an even more prominent peak at ~26 eV is observed for the $\pi + \sigma$-plasmon. The shoulders between ~8 and ~25 eV have been attributed to transitions between bonding σ and antibonding σ^* levels, and partially also to mixed $\pi - \sigma^*$ or $\sigma - \pi^*$ transitions [234]. Through the Kramers-Kronig analysis (see Sec. 2.3.2), these, as well as other less pronounced details of the EELS loss spectrum, enter into the complex dielectric function $\varepsilon(\omega)$ as features between 7 eV and 40 eV. It should be noted that the peak positions in $\varepsilon''(\omega)$ (at 7.7, 8.9, 10.0, and 12.2 eV) obtained by analyzing the EELS data are in agreement with the optical UV results reported by Kelly *et al.* [237] using a synchrotron radiation ellipsometer. The higher energy feature at 21.5 eV may be associated with the *giant optical absorption* that was detected around 21 eV in the gas phase of both C_{60} and C_{70}, via photoionization spectroscopy using synchrotron radiation [239]. Not shown on Fig. 4-1 are the results of XPS and UPS experiments at much higher frequencies (~300 eV) probing the core electrons of C_{60} solid and thus contributing to the core dielectric constant ε_∞.

From Fig. 4-1, it is clear that, as we move towards lower and lower frequencies, for every loss process represented by a peak in the $\varepsilon''(\omega)$, there is a rise (sometimes accompanied by a small oscillation) in $\varepsilon'(\omega)$, as prescribed by the Kramers-Kronig relations. As we move below 10^{13} Hz, all electrons and most phonons have already responded, and $\varepsilon'(\omega)$ is approaching its DC value. The small difference between $\varepsilon'(10^{13}\,\mathrm{Hz}) \approx 3.9$ [61] and $\varepsilon'(10^{5}\,\mathrm{Hz}) \approx 4.4$ [24] (shown by an arrow in Fig. 4-1) is probably due to the losses associated with C_{60} molecules rapidly rotating at room temperature ($T > T_{01}$) at $\sim 10^9$ Hz, as evidenced by NMR [73], ultrasound attenuation [52], and other experiments sensitive to phenomena in this frequency range (see Sec. 1.3.2).

From the Kramers-Kronig relations, it follows [see Eqn. (2.38)], for the case of zero frequency:

$$\varepsilon'(0) - 1 = \frac{2}{\pi}\int_0^\infty \frac{\varepsilon''(\omega)}{\omega}\,d\omega = \frac{2}{\pi}\int_0^\infty \varepsilon''(\omega)\,d(\ln\omega). \tag{4.4}$$

This tells us that the DC dielectric constant $\varepsilon'(0)$ includes *all* contributions from the higher frequency loss processes, and is proportional to the area under the $\varepsilon''(\omega)$ curve plotted on a logarithmic scale [177]. The rest of this chapter reports the measurements of the dielectric function $\varepsilon(\omega)$ of C_{60} thin films for frequencies *below* 10^5 Hz, where new, previously unreported, polarization mechanisms come into play.

4.3 Experimental difficulties in obtaining intrinsic electrical characteristics of C_{60} solids

One of the fascinating peculiarities of solid fullerene materials is the fact that their properties can be greatly affected by a host of external factors — from ambient gases to ambient light. These effects are important for both optical and electrical measurements. In particular, the results of electrical measurements (*e.g.*, transport, dielectric properties, photoconductivity) can be affected by many orders of magnitude.

The realization of the importance of external factors when measuring electrical and optical properties of fullerites has not always been appreciated by the fullerene research community, which led to the appearance of dozens of erroneous reports in the literature on electrical and other properties (particularly, photoconductivity) of C_{60} and other fullerites. After three years of experimental research into the properties of solid C_{60}, we have identified the following four major effects peculiar to fullerene solids that tend to skew the results of electrical and optical measurements:

Large Interstitial Volume: A large amount of interstitial volume (26% for close-packed spheres) leads to rapid uptake of molecular oxygen and other impurities from the ambient environment. Such impurities quench carrier transport and photoconductivity in solid C_{60}, greatly affecting the measurements of these properties. Due to the possibility of charge transfer from an impurity to a C_{60} ball, large dipole moments are created that affect the dielectric measurements.

In addition, the mobile impurities complicate many electrical measurements by lowering the breakdown voltage of the C_{60} films, so that these measurements need to be performed at low voltage levels, which results in decreasing the signal-to-noise ratio.

Phototransformation: As was described in Sec. 1.3.2 (page 37), C_{60} films photopolymerize easily when irradiated with vis-UV light. Any experiments involving high-intensity light (*e.g.*, photoconductivity, pump-probe reflectivity or transmission [240], etc.) should, therefore, be performed with caution, so as to avoid polymerization of the film. In addition, UV light facilitates adsorption of oxygen into the bulk of the film (see Sec. 4.4.1), leading to the undesirable consequences outlined above.

Long-lived excited states: It has been shown by Hamed *et al.* [241] that C_{60} films exhibit *persistent photoconductivity,* the effect which consists of a metastable increase in dark conductivity caused by brief exposure to light. This points to the existence of long-lived (with time constants on the order of days) excited states in solid C_{60} (attributed to the distortions that the C_{60} molecules experience in the presence of localized charge [241]). Occupation of these excited states increases the effective conductivity of C_{60} films by many orders of magnitude.

Crystallinity: The properties of C_{60} films change substantially depending on their degree of crystallinity. Single-crystal films would come closest to the intrinsic bulk properties of crystalline C_{60}. However, the difficulties in manufacturing such films (MBE or Langmuir-Blodgett techniques are necessary to obtain films of high crystallinity), prompted us to turn to vacuum-deposited polycrystalline films (see Sec. 4.5 and the HRTEM photo in Fig. 1-14) for our investigations. The degree of crystallinity can be monitored using X-ray diffraction (see Fig. 4-11). It should be noted that the crystallite size distribution of the polycrystalline films is strongly affected by the nature of the substrate [112], and under certain conditions, the films can even be made completely amorphous.[1]

From the preceding discussion, it might appear that it is virtually impossible to obtain the properties of pristine C_{60} by investigating a C_{60} film. Indeed, any C_{60} experiment calls for a C_{60} film to be made and kept in vacuum (to avoid impurities "polluting" the fullerite's large interstitial regions), in complete darkness (to avoid phototransformations), for days prior to the start of and during the experiment (to allow the long-lived excited states to die out). The experiment itself needs, of course, to be performed in vacuum to protect the films from contamination with ambient impurities.

The practical reality rules out the possibility of such a complicated experimental setup. While we tried to keep exposure to the ambient light and atmosphere to a minimum, it was practically impossible to completely eliminate either of the two. Instead, we directed our efforts toward developing methods to continually monitor the status of the film (impurity concentration, degree of polymerization, etc.) and then use this information to deduce the behavior of the pristine film. Microdielectrometry (described in Chapter 3) is one method particularly suitable for this task.

4.4 Film modification: Motivation and justification

While C_{60} may be a desirable material for use in electronic devices (*e.g.*, as a gate dielectric — see Sec. 1.7), its dielectric properties are easily compromised by the presence of large interstitial spaces which can be easily filled with mobile polar impurities, as described in Sec. 4.3 above. The need to prevent the diffusion of such impurities

[1]Crystallinity of the vacuum-grown films is also strongly affected by the temperature of the substrate during deposition. In a systematic investigation of this substrate temperature effect, Rusakova *et al.* [242, 243] found that a relatively small change in substrate temperature from 40°C to 200°C can increase the grain size by an order of magnitude from 25 nm to 250 nm.

into the bulk of a C_{60} solid prompted us to attempt to engineer a C_{60}-based material in which most of the interstitial spaces are closed (filled), and thus are inaccessible to external impurities.

We devised and tested two different ways for filling the interstitials of a C_{60} film.

In one approach, an external "filler" or "glue" molecular species is forced into the interstitials of a C_{60} solid. Oxygen (O_2) is one molecular agent that is known to diffuse into C_{60} films either under pressure [244, 245] or with the assistance of UV irradiation [116, 117, 246, 247], as described in Sec. 4.4.1 below. Some species, when forced into a C_{60} solid's interstitials, will react with surrounding C_{60} balls, forming compounds extending through (and thereby "sealing off") the interstitial spaces of a fullerite. Direct reactive oxygenation (*e.g.*, using ozone) is one method belonging to this class of techniques. Other related methods include chlorination [248], bromination [248], and fluorination [92]. Another molecule that shows much promise as a molecular "glue" yielding a range of electrically remarkable C_{60}-based materials is NO (nitric oxide) [139]. Its small size (1.1508 Å) allows it to easily diffuse into the bulk of the fullerite, and its substantial dipole moment (0.16 Debye) enhances the dielectric constant of the resulting compound considerably. The results obtained by intercalation of these species into C_{60} films are presented in Sec. 4.10.

A completely different method of "sealing off" the interstitials of a fullerene solid is to use C_{60}'s propensity to crosslink and polymerize when exposed to intensive UV-vis irradiation [45], thereby reducing (or, perhaps, even eliminating) the interstitials into which impurities may diffuse. We measured the dielectric properties of UV-polymerized C_{60} films, as well as those grown (deposited) in the presence of UV radiation, and compared them to the results obtained with pristine C_{60} films (see Sec. 4.10).

4.4.1 NMR and ESR evidence for oxygen diffusion

Since oxygen has proved to be one of the most important intercalants affecting the electrical properties of C_{60} films, it is worthwhile to discuss the evidence for oxygen intercalation into the bulk of C_{60} solid in more detail.

It was mentioned in Sec. 1.5 that oxygen can be an exohedral intercalant of C_{60} solids (see Fig. 4-2). Unlike the alkali-metal intercalants, which can transfer a large amount of charge (the outer shell electron for each alkali-metal atom) to the C_{60} balls, virtually no such charge transfer can be assumed for the case of oxygen intercalation. However, some charge transfer does indeed occur, giving rise to the enhanced polarization effects described in Sec. 4.7. It will be shown in Sec. 4.7 that the amount of charge transferred by oxygen molecules is between 20 and 100 times less than that transferred by alkali-metal atoms.

A variety of experiments provide evidence for oxygen diffusion in fullerites. Assink *et al.* [244] have used ^{13}C NMR spectroscopy to show that molecular oxygen diffuses readily into the octahedral interstitial sites of the fcc lattice of C_{60}. As shown in Fig. 4-3, exposure of C_{60} to 1 kbar oxygen for 1.75 hours at room temperature resulted in a spectrum of seven evenly spaced resonances corresponding to the filling of 0 to 6 of the adjacent octahedral interstitial sites with oxygen molecules. Oxygen pressure was found to substantially accelerate the rate of oxygen diffusion [Fig. 4-3(b)], but it was also observed that, even at ambient conditions, oxygen eventually fills much of the octahedral sites of a fullerite. The exact proportion of the sites filled depends very substantially on the crystallinity of the sample, as discussed in Sec. 4.3. Crystalline powders with micron-sized crystallites, such as those used by Assink *et al.* [244], tend to have considerably lower diffusion rates than the vacuum-deposited polycrystalline films composed of much finer crystallites that were used in our study (see Sec. 4.5 for the details of sample preparation and characterization).

While forcing oxygen into the interstitials of a fullerite under pressure is an obvious method of speeding up the diffusion, its practical significance is quite limited. UV-

Figure 4-2: C_{60} molecules (green) arranged in a face-centered cubic lattice. Oxygen molecules (O_2, red) occupy octahedral interstitial sites of the C_{60} solid. The carbon atoms (green) and oxygen atoms (red) are represented by spheres of radii corresponding to the van der Waals radii of carbon and oxygen, respectively. This figure was created on a Silicon Graphics Indy^{TM} workstation running *Cerius*^{2} software by Molecular Simulations, Inc.

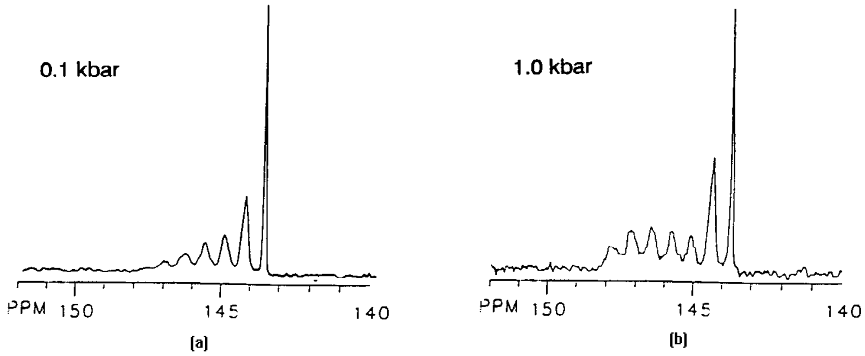

Figure 4-3: NMR evidence for pressure-assisted oxygen diffusion into C_{60} films. The largest peak in both (a) and (b) corresponds to the primary resonance at 143.7 ppm corresponding to an fcc C_{60} solid at $T > T_{01}$. The other six peaks correspond to the C_{60} molecules in the lattice surrounded by 1, 2, 3, 4, 5, and 6 oxygen molecules, respectively. Spectra (a) and (b) were taken for samples exposed for 1.75 hours to 0.1 and 1.0 kbar oxygen, respectively [244].

assisted oxygen diffusion [117, 247] provides a more expedient means of forcing the oxygen into the bulk of C_{60} solid. (Indeed, this method has been used in a C_{60}-based negative-photoresist photolithography process, as described in Sec. 1.7.6.) Eloi *et al.* [117] verified the increase in the diffusion rate of O_2 into the fcc C_{60} lattice by direct measurement of the oxygen uptake via resonant alpha particle scattering experiments, as shown in Fig. 4-4. The broadening of the resonance scattering peak in Fig. 4-4(b) indicates that a thin (20 nm) oxygen layer with a composition of $C_{60}O_{0.6}$ (corresponding to about one oxygen molecule per two C_{60} balls) was formed on the surface of the C_{60} film upon UV irradiation in 1 atm of O_2. Eloi *et al.* [117] showed that, depending on the intensity of the UV irradiation, the stoichiometry of the surface layer of a C_{60} film can reach oxygen concentrations as high as $C_{60}O_{4.8}$. Since there is only one octahedral site ($R_{\text{octahedral}} = 2.07$ Å; see Table 1.2) per C_{60} molecule in the fcc lattice (see Fig. 4-2), *physisorption* of molecular oxygen in the lattice would result in a maximum oxygen stoichiometry $C_{60}O_2$. Furthermore, the possibility of molecular oxygen occupying the tetrahedral sites ($R_{\text{tetrahedral}} = 1.12$ Å; see Table 1.2)

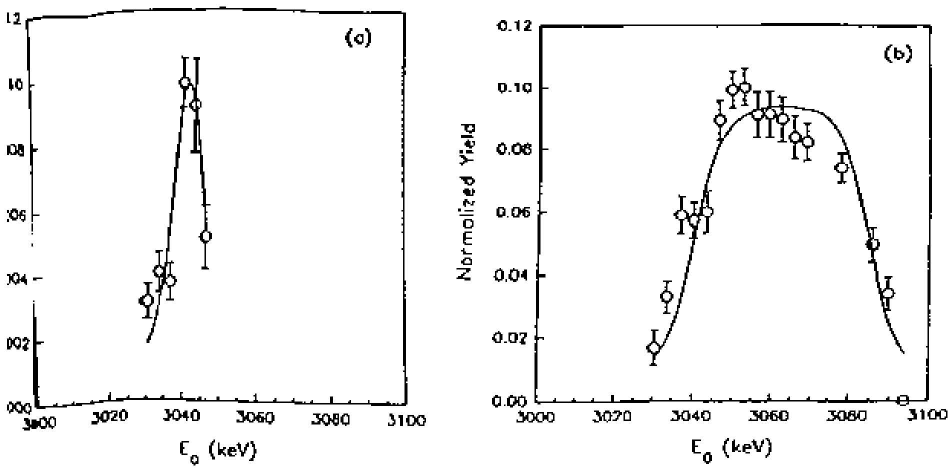

[a] [b]

Figure 4-4: Resonant alpha particle backscattering evidence for UV-assisted oxygen diffusion into C_{60} films. Oxygen excitation yields obtained from a resonance scan of a 1400 Å thick C_{60} film exposed to 1 atm O_2 for 1 hr in the absence of light (a), and from a 2400Å thick film which was simultaneously exposed to 1 atm O_2 and light from a Xe lamp for 1 hr (b) [117].

is eliminated by considering that the van der Waals radius of an oxygen molecule is 1.4 Å, too large to fit into a tetrahedral site. Stoichiometries higher than those expected from simple physisorption (*e.g.*, pressure-induced diffusion, as described above) can be attributed to a subsequent chemical reaction between the C_{60} and oxygen under continued irradiation.

Electron Spin Resonance (ESR) spectroscopy is another method for assessing the oxygen content of C_{60} films. Neutral fullerenes (C_{60}) in their ground state are in a singlet state. Compensated spins are also expected in CO, CO_2, $C_{60}O$, $C_{60}O_2$, $C_{60}O_4$. In principle, this inhibits the use of ESR. Nonetheless, it was noted that the "as-grown" fullerenes are weakly ESR-active [249, 250], and also that unpairing of the electron spins occurs in C_{60}:O_2 solid mixtures under UV irradiation [251]. This makes ESR a good method for studying the oxygen content of UV-irradiated films. Figure 4-5 follows the evolution of the unpaired spin concentration in a typical 914 Å-thick C_{60} film used in our dielectric studies. As seen in Fig. 4-5, the spin concentration increases rapidly under UV-exposure in 1 atm of oxygen, reaching near-saturation levels within about 3 hours. Subsequent exposure in vacuum partially reverses this effect, expelling about a third of adsorbed oxygen within an hour. Annealing the film in vacuum at 175°C reverses the effect completely. (The effect of annealing on the transport properties of C_{60} films is discussed in Sec. 4.4.2.)

It is important to emphasize that, while oxygen does indeed diffuse into the bulk of fullerites, profoundly affecting their electrical and optical properties, many other molecular intercalants that have been investigated do not. In particular, it has recently been reported [252] that considerably more O_2 is intercalated into the C_{60} lattice than in the case of N_2 under identical experimental conditions, despite the fact that the sizes of the two molecules are quite similar. This real difference in the behavior of O_2 from that of N_2 has significant technological implications, as it could lead to techniques for separating these two gases — a goal of considerable practical

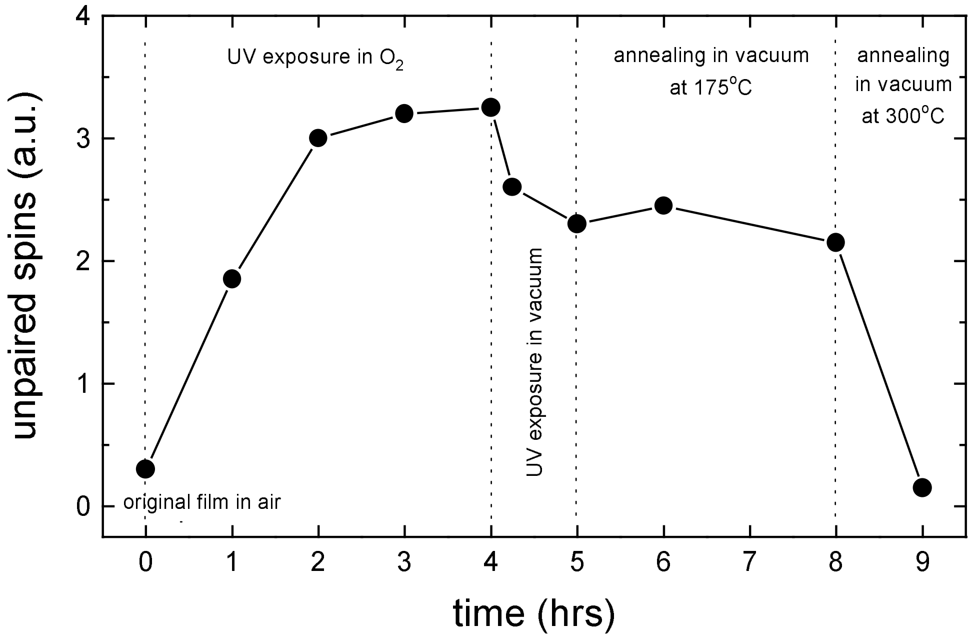

Figure 4-5: ESR evidence for UV-assisted oxygen diffusion into a 914 Å C_{60} film. (Data courtesy Dr. S. Glarum of AT&T Bell Labs.)

importance.[2]

4.4.2 Transport Evidence of Oxygen Diffusion

Given the exponential dependence of conductivity on the position of the Fermi level in a semiconductor, conductivity measurements can provide an extremely sensitive way of monitoring the density of electronic states in the gap or near the band edges of crystalline C_{60} caused by oxygen, light, or other agents. In particular, as mentioned in Sec. 4.3, oxygen decreases the intrinsic conductivity of fullerites by as much as four orders of magnitude. The magnitude of this effect, together with C_{60} solid's

[2]While not quite as technologically important — and indeed not quite as unexpected, — we have also found that Xe, a heavy noble gas with a van der Waals radius comparable to that of C_{60} lattice interstitials, can be made to diffuse into a C_{60} crystalline powder, as evidenced by the weight uptake. By subjecting C_{60} powder to a Xe environment at $T = 200°\mathrm{C}$ and $p = 850$ psi for 2 days, the composition of $C_{60}Xe_{0.203}$ was achieved. However, Xe atoms were found to promptly pop out of the C_{60} interstitials once the pressure is removed.

σ at 300 °C (S/cm)	E_a (eV)	Ref.
$\sim 10^{-6}$	0.26	[253]
1.7×10^{-7}	0.58	[60]
4×10^{-7}	0.36	[254]
$\sim 10^{-4}$	0.26	[255]
$\sim 10^{-8}$	0.43	[256]
$\sim 10^{-14}$	1.1 (↓)	[257]
8.3×10^{-7}	0.54 (↑↓)	[258]
$\sim 10^{-11}$	1.0 (↑), 0.5 (↓)	[121]
2×10^{-8}	0.51	[122]
5.4×10^{-10}	~1 (↑↓)	[259]
$\sim 10^{-14}$	0.82	[260]
3×10^{-10}	0.51	[261]

Table 4.1: Intrinsic conductivity σ and activation energy E_a reported for C_{60} single crystals and highly crystalline films (top portion), and for polycrystalline and amorphous films (bottom portion). E_a is the activation energy for temperatures above the structural transition $T_{01} > 260$°C, measured on heating (↑) and/or on cooling (↓), when specified by the data source.

propensity for adsorbing oxygen from the surrounding atmosphere, is responsible for the wide dispersion of values for the conductivity of C_{60} reported in the literature.

Table 4.1 summarizes the results for experimental values of C_{60} conductivity reported in 12 papers on the subject. These papers were chosen so as to exclude those whose authors displayed lack of awareness about the profound effect of oxygen on the electronic properties of solid C_{60}. All of the values in the Table 4.1 are purported to display the *intrinsic* conductivity of C_{60} films and crystals. Still, a quick glance at Table 4.1 confirms that the reported results for σ vary by as much as ten orders of magnitude.

To characterize the conductivity (and, by inference, the oxygen content) of our C_{60} films, we have performed transport measurements using the Micron sensor and the measurement technique described in Sec. 3.3 and 3.4, respectively. Typically, a 2000 Å-thick C_{60} film was deposited on the sensor as described in Sec. 4.5, and its conductivity was measured for temperatures ranging from 25 °C to 250 °C, as shown in Fig. 4-6(a). The average temperature scanning rate was ~1 °C for every five minutes. The arrows in Fig. 4-6 indicate the direction of the temperature sweep. The current amplifier setup described in Sec. 3.4 allowed us to monitor the change in conductivity over seven decades. The measurement was performed at $V = 1$ V, and the conductivity σ was calculated using Equations (3.10) and (3.12).

We notice right away that annealing increases the conductivity of C_{60} film, probably both by improving the crystallinity of the film and by driving the oxygen out of the interstitial regions.

Typically, the conductivity is activated in accordance with the Arrhenius equation of the form

$$\sigma = \sigma_0 \exp\left(-\frac{E_a}{kT}\right), \tag{4.5}$$

where σ_0 is the conductivity prefactor, k is the Boltzmann constant, T is the absolute temperature, and E_a, the activation energy, is a measure of the energy distance between the Fermi level and the band edge in the semiconductor. In the case of a crystalline solid, the conductivity is determined by thermal excitation of charge carriers over the energy gap, and the activation energy should be approximately half of the value of the band gap. Figure 4-6(b) displays an Arrhenius plot of the conductivity.

The kink in the curve at $T \approx 120$ °C during the temperature up-sweep probably corresponds to the onset of oxygen effusion. Region 1 of the curve thus corresponds to the oxygen-filled C_{60}, which has a conductivity exhibiting an activation energy of $E_a = 0.44$ eV. Above $T \approx 120$°C (region 2 of the curve), oxygen is expelled out of the C_{60} solid. This process is also activated in temperature, and it affects the conductivity of the film, thus the activation energy of the effusion adds to the activation energy of oxygenated C_{60}, yielding a relatively high (in the view of the C_{60}'s HOMO-LUMO gap of ~1.6 eV) value $E_a = 1.90$ eV.[3]

[3]Since oxygen molecules leaving C_{60} film no longer participate in the C_{60} transport mechanisms (*e.g.*, as carrier traps), the number $E_a = 1.90$ eV for the combined activation energy of transport

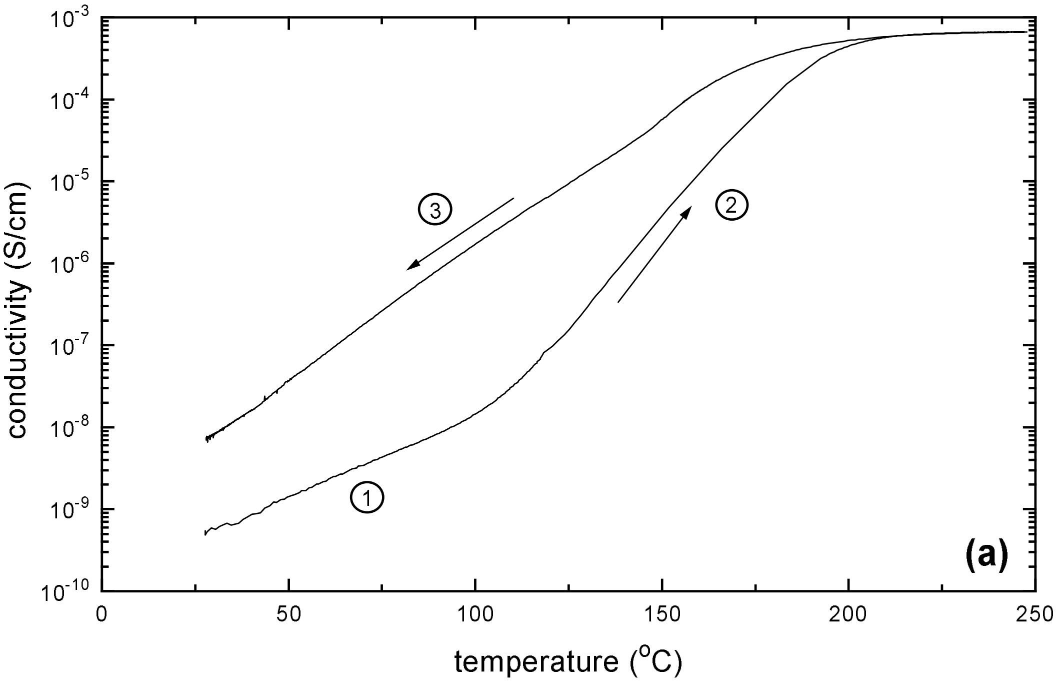

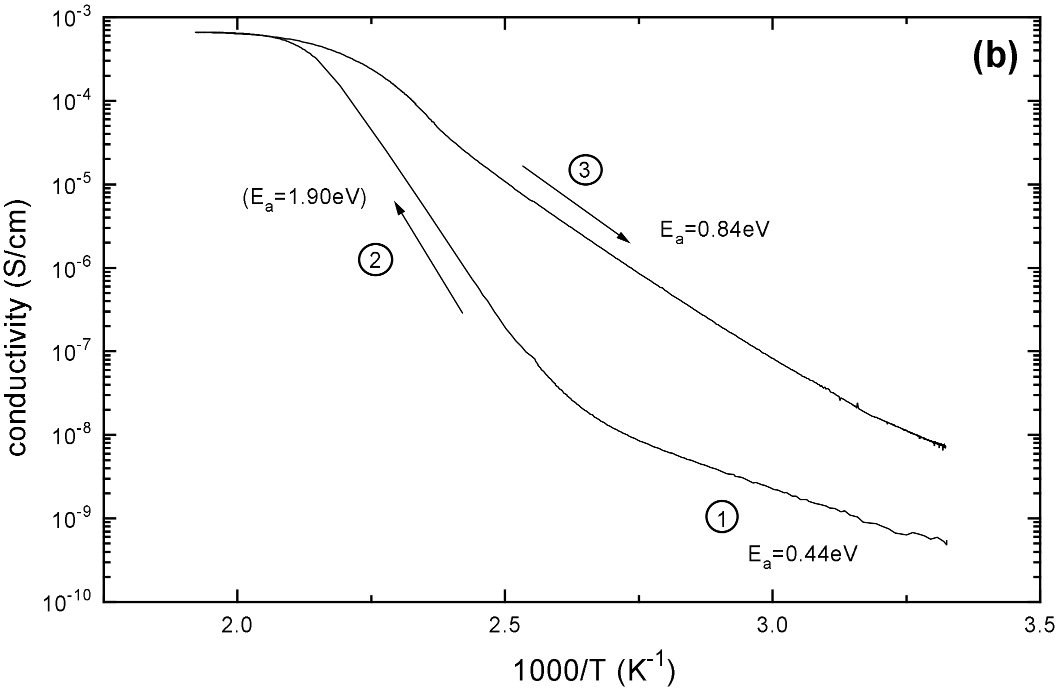

Figure 4-6: Transport measurements of C_{60} film. The measured Conductivity of C_{60} is plotted versus temperature (a) and vs 1000/T on an Arrhenius plot (b). Arrows indicate the direction of temperature scan.

The curves in Fig. 4-6 level off at ~220°C, as C_{60} molecules start to sublimate from the substrate (a first-order phase transition). Although the accepted value for the sublimation temperature of C_{60} is ~350°C [63] (see Table 1.2), it has been our experience that the onset of sublimation occurs at temperatures as low as 200°C. Region 3 of the curves in Fig. 4-6 following the annealing, where the conductivity is activated with $E_a = 0.84$ eV, corresponds to de-oxygenated C_{60} rapidly adsorbing oxygen. Since this is a transient process, no reliable determination of the intrinsic activation energy of C_{60} can be made from these data.

Note that those conductivity studies listed in Table 4.1 reporting conductivities lower than the average also report activation energies higher than the average. It is fairly certain that the amount of adsorbed oxygen played a large role in those studies, rendering their conclusions highly questionable. While not providing the final word on the role of oxygen in the electronic transport, our study yields results consistent with the accepted conductivity value of 1.7×10^{-7} S/cm [60] (see Table 1.2), supports the observations of reversibility of oxygen diffusion with annealing [244, 255], and provides an explanation for the erroneous values for the conductivity and the corresponding activation energy reported in the literature (see Table 4.1).[4]

It has been speculated [255] that oxygen affects the transport properties of the C_{60} films in at least two distinct ways. In the first few minutes of exposure, oxygen diffuses through the inter-grain boundaries, rapidly quenching electronic transport, and decreasing the intrinsic conductivity of C_{60} by one or two orders of magnitude. Then, in a slow process that can run for hours or even days, oxygen diffuses into the interstitial spaces of the fullerite crystallites, lowering the conductivity of the material by about two more orders of magnitude. While this theory appears plausible and consistent with our study, more experiments are needed to ascertain the effect of

---

and effusion has no straightforward interpretation.

[4]After the present work had been completed, an excellent paper by Asakawa *et al.* [262] came to our attention, in which our conclusions regarding oxygen effects on conductivity and activation energy have been confirmed in a careful *in-situ* experiment.

oxygen on electronic transport in the fullerite. Additional evidence supporting and extending this theory is provided by our studies of low frequency dielectric properties of fullerene thin films reported in Sec. 4.7.

4.5 Sample preparation and characterization

All samples used in this study were prepared at AT&T Bell Laboratories at Murray Hill, NJ, in the lab of Dr. Arthur Hebard. In this section we review the general techniques and considerations related to preparing and characterizing thin film fullerite samples.

Generally, when planning a thin-film experiment extending to cryogenic temperatures, particular attention should be paid to choosing the substrates.[5] Ideally, the substrate used for measuring the electrical properties of a material versus temperature should possess the following properties:

1. High electrical resistivity, to prevent parasitic currents and capacitances arising between the sample and the substrate from skewing the measurements.

2. High thermal conductivity, to afford good cryogenic control, particularly in situations when external incident radiation is present (such as in *in situ* optical measurements of C_{60} — photoconductivity, pump-probe experiments, and polymerization experiments).

3. The thermal expansion coefficient matched with that of the film being measured, to avoid cracking and tearing apart the film.

For our C_{60} experiments, we have used quartz, fused quartz, and glass (pyrex) substrates, all of which are excellent insulators. From Fig. 4-7, it is evident that, when

[5]This discussion is limited to choosing substrates suitable for electrical measurements. A different set of criteria for choosing a substrate should be applied in preparing a spectroscopy experiment. In this context, the ideal substrate (for a transmission experiment) is one that is transparent to the incident radiation. For example, KBr or Si substrates are usually used in infrared spectroscopy; quartz substrates — in UV-vis spectroscopy, and sapphire substrates — in X-ray diffraction experiments.

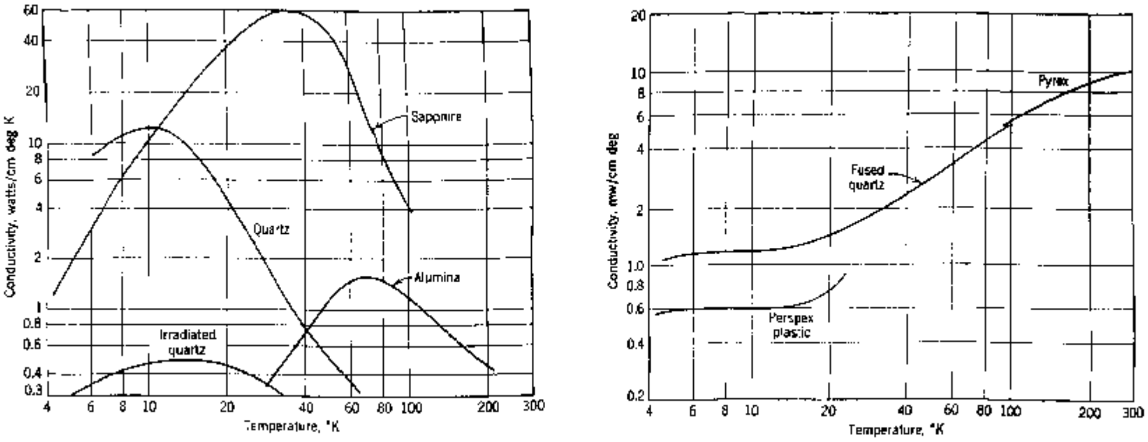

Figure 4-7: (a) Thermal conductivity of a number of electrically insulating solids as a function of temperature, plotted on a log-log scale. The log-temperature scale is used to emphasize the practically important behavior of the thermal conductivity at cryogenic temperatures. (b) Thermal conductivity for glass (pyrex), fused quartz, and Perspex plastic, plotted on a log-log scale. Note the change in scale of the ordinate.

high thermal conductivity is important (*e.g.*, in optical experiments), a quartz substrate is much preferable, as its thermal conductivity can be up to four orders of magnitude higher that that of pyrex or fused quartz (at ~10 K).[6]

As described in Sec. 3.3, the integrated and 1-micron interdigitated sensors, which were used for some of the dielectric and transport experiments described below, are patterned on silicon and quartz, respectively. From Table 3.1, their operating temperature ranges are -100–250°C and -150–200°C, respectively, with the 1-micron sensor capable of sustaining temperatures as low as 10 K.

For thin-film deposition, 10–15 mg of 99.9% purified C_{60} (most batches were supplied by Dr. Robert Haddon of AT&T Bell Laboratories, with the rest coming from

[6]The substrate thermal conductivity considerations are even more important in optical measurements of superconducting samples, such as the alkali-metal-doped M_3C_{60} (M=K,Rb,Cs) films that turn superconducting with critical transition temperatures T_c ranging from 18 K to 40 K (see Sec. 1.5). A pump-probe measurement on such films is currently being performed by us at MIT [240, 263], with films prepared at Bell Labs on sapphire substrates. As is clear from the Fig. 4-7(a), sapphire is the best available insulating material (as far as thermal conductivity is concerned) in the temperature range of 10–100 K.

Hoechst AG, a commercial supplier) were loaded into alumina crucibles. The rotating substrate (either at ambient or at elevated temperature, up to ~200°C), was located approximately 10 cm from the crucibles, and a quartz-crystal microbalance was used to monitor the rate of deposition and final film thickness (see Fig. 4-8). A 200°C soak cycle with shutter closed over the substrate prevented high vapor pressure solvent residues from reaching the substrate. Using a diffusion pump connected to the deposition chamber, a base pressure of 1.5×10^{-6} torr was maintained during the deposition. Deposition rates in the range of 5–30 Å/min were typical for source temperatures of ~350°C. After the deposition, the thickness of the films was determined by ellipsometry (or by profilometry, for thicker films), and was generally found to be in good agreement with the readings of the thickness monitor (see Fig. 4-9).

Confirmation that the deposited films comprise C_{60} molecules has been obtained from the infrared transmission and UV-vis absorbance spectra shown in Figs. 4-10(a) and 4-10(b), respectively. X-ray powder diffraction (Fig. 4-11) was used to ascertain the fcc structure of the C_{60} crystallites comprising the film. Small crystallites on the order of 100 Å in diameter were typical. High resolution transmission electron microscopy (HRTEM) was utilized to further visualize the morphology of the film (see Fig. 1-14).

Raman spectroscopy was also employed for film characterization, with results similar to those presented in Fig. 1-21. In particular, it was confirmed that our films did indeed phototransform (polymerize) when irradiated with high intensity 488 nm light (Fig. 4-12).

In order to assess the oxygen content of our films, electron spin resonance (ESR) and weight uptake techniques were used, as discussed in Sec. 4.4.

To investigate the electrical properties of our C_{60} films, we fabricated Al-C_{60}-Al trilayer structures for electrical characterization (Fig. 4-13). These sandwich structures were made by depositing in succession on glass: 200 μm-wide aluminum down stripes, a known thickness of C_{60}, and finally, 200 μm-wide aluminum cross stripes.

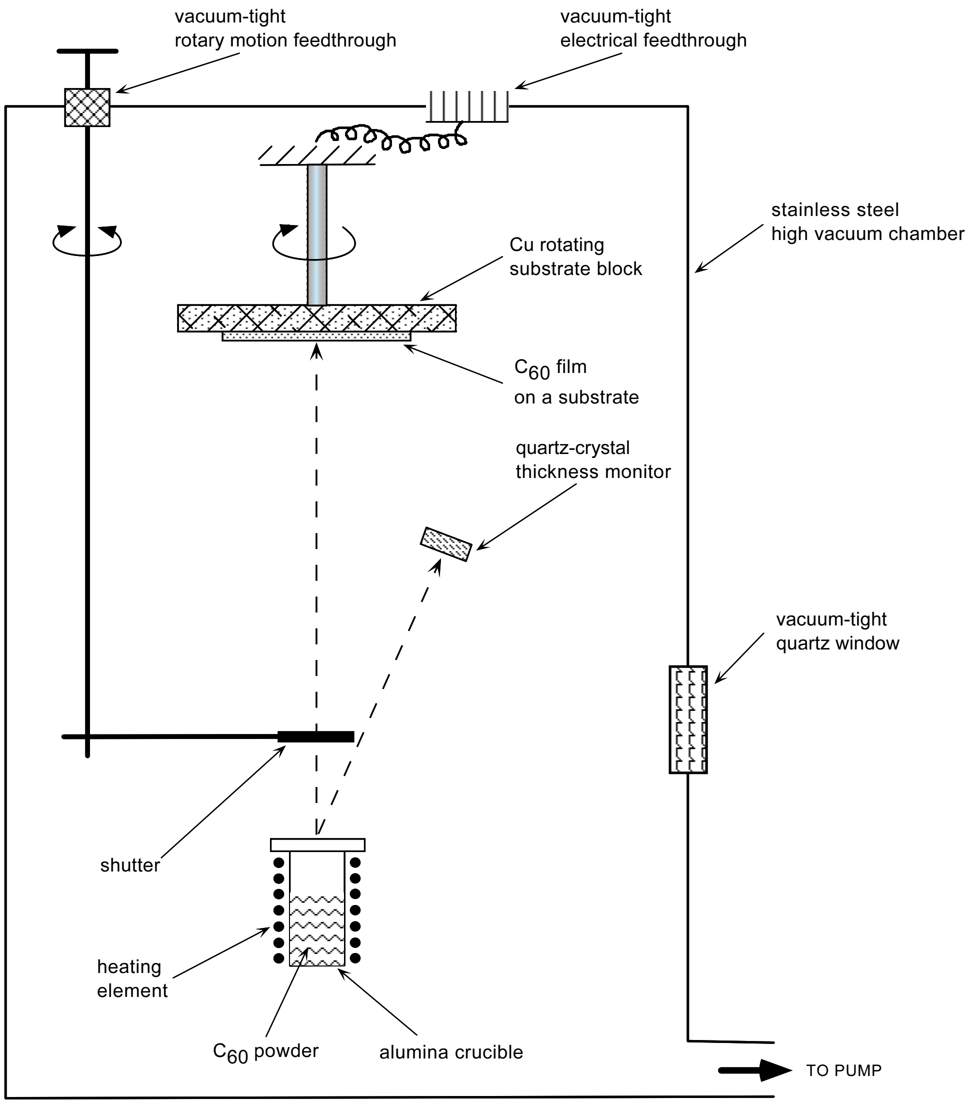

Figure 4-8: A schematic of the vacuum deposition system used to grow the C_{60} films for all experiments described herein. The system is located at AT&T Bell Labs, in the laboratory of Dr. Arthur Hebard.

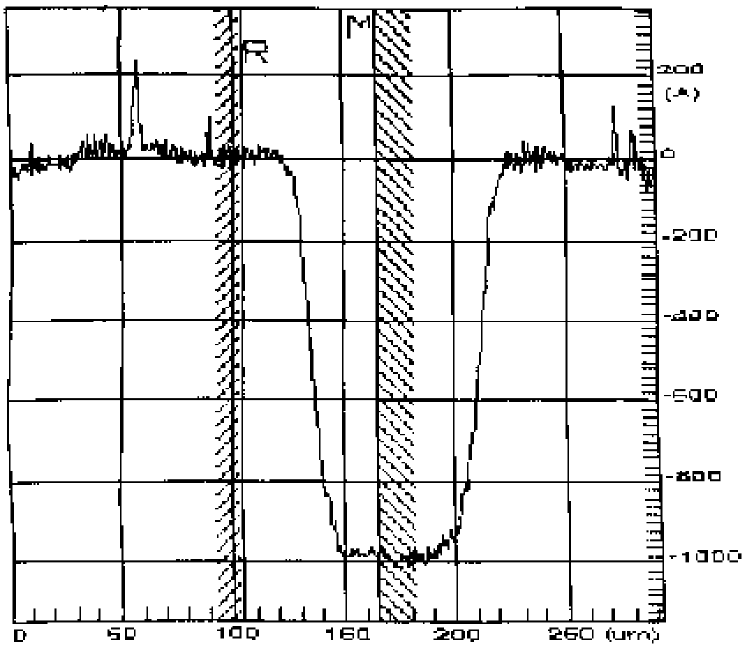

Figure 4-9: A Dektak 8000 profilometer measurement of a 1000 Å C_{60} film (as indicated by the crystal monitor in the deposition system depicted in Fig. 4-8). A narrow ($\sim 70\mu$m) channel was masked on the surface of the substrate with a thin gold wire prior to the C_{60} deposition. After the deposition, a profilometer scan was taken across the resulting gap in the film. To avoid scratching the film, a light profilometer stylus was used, exerting the force of only 12 mg on the surface of the film. The depth measurement taken between the two vertical diagonally shaded bars shown on the plot indicated a film thickness of 989 Å, in close agreement with the expected thickness of 1000 Å. [The Dektak 8000 profilometer used for these measurements is located at the Microfabrication Shared Educational Facility of the MIT Center for Material Science and Engineering (CMSE).]

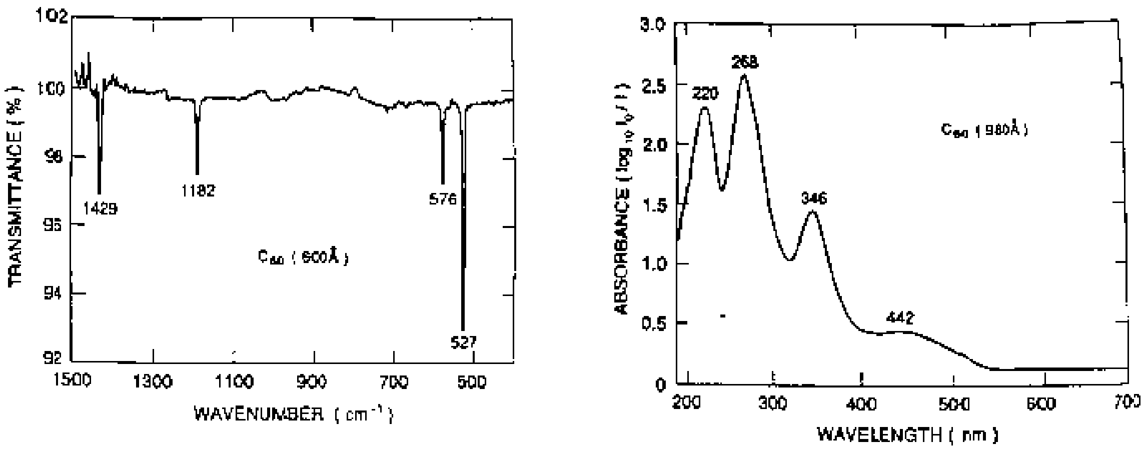

Figure 4-10: (a) Infrared transmission of a 600 Å-thick C_{60} film deposited on a KBr substrate. The frequencies of the four absorption peaks labeled on the figure [*cf.* Fig. 1-21(a)] coincide with other published values for sublimed films [7, 45] and are also seen for C_{60} in solution, pointing to the molecular character of the C_{60} solid films. (b) Wavelength-dependent absorbance of a 930 Å-thick C_{60} film deposited onto quartz. The four prominent absorption peaks arise from interband transitions among the molecular orbitals [24].

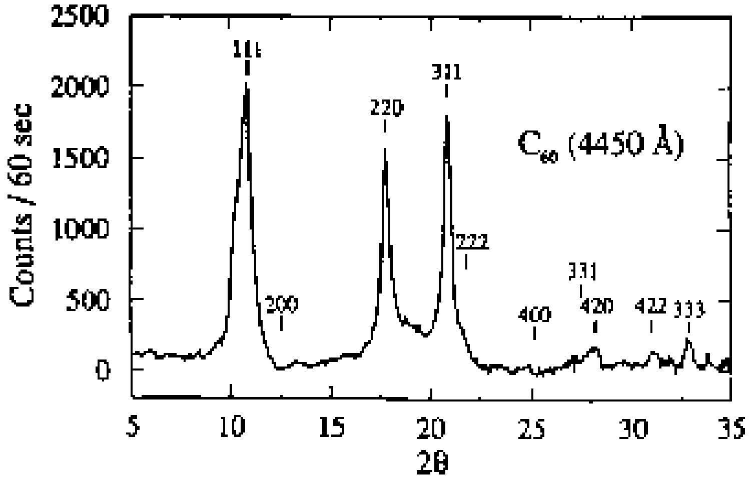

Figure 4-11: X-ray scan of a 4450 Å-thick C_{60} film deposited onto an off-axis cut single-crystal sapphire substrate. The markers indicate the calculated diffraction lines from a face-centered cubic cell seen in diffraction from bulk C_{60} powder. The flat background indicates that the film does not have a significant amorphous fraction. The width of the peaks indicates that the crystalline domains do not have long-range order (the film is polycrystalline), with the coherence length on the order of 60 Å, or about four unit cells [24].

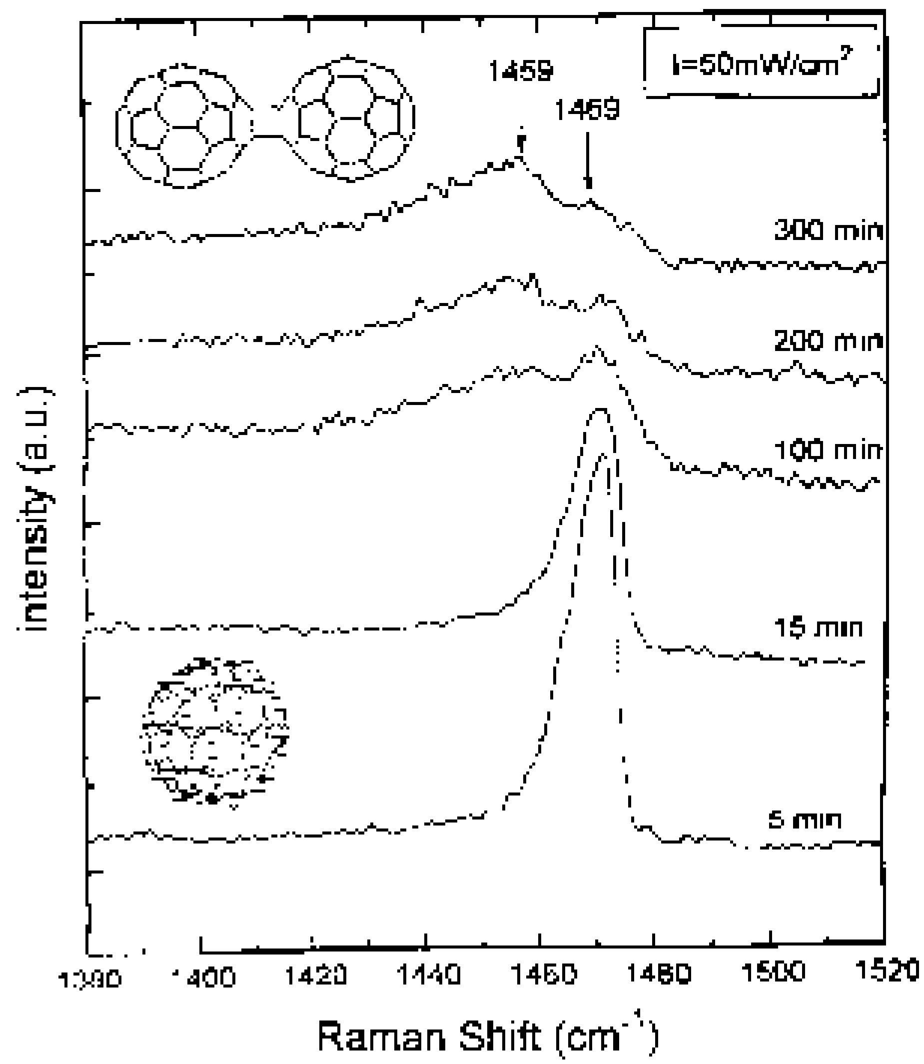

Figure 4-12: The characteristic signature of the C_{60} photopolymerization process is the gradual shift of the 1469 cm^{-1} Raman $A_g(2)$ line (corresponding to the pentagonal-pinch vibrational mode in C_{60} before polymerization, see Sec. 1.6) to 1459 cm^{-1}. This figure follows the decay of the 1469 cm^{-1} Raman peak and the development of the 1459 cm^{-1} peak in a vacuum-sublimed 1000 Å-thick C_{60} film subjected to 50 mW/cm^2 argon-ion laser irradiation at 488 nm. The decreased magnitude of the Raman peak at 1459 cm^{-1} in photopolymerized C_{60} film compared to the original 1469 cm^{-1} peak in pristine C_{60} points to increased disorder due to polymerization. This Raman study was performed at the Francis Bitter National Magnet Laboratory (M.I.T.)

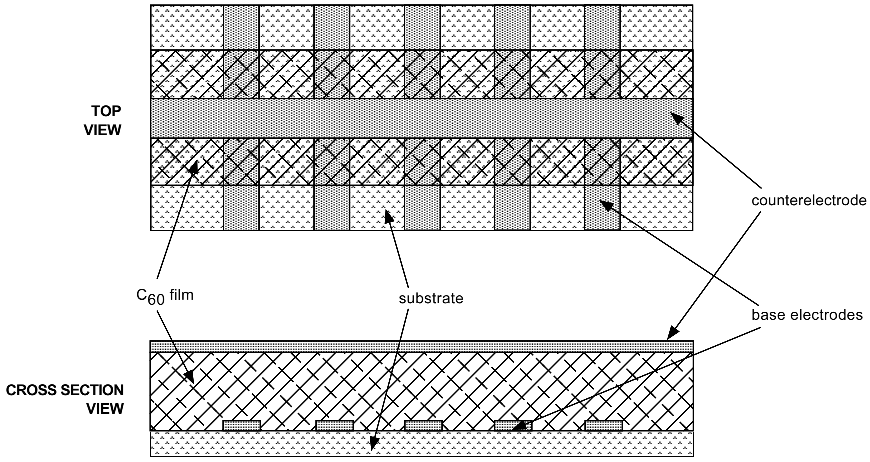

Figure 4-13: A typical trilayer ("sandwich") structure is composed of five identical Al-C_{60}-Al junctions, each of which can be used independently in a dielectric (or transport) experiment.

The sample was briefly handled in the ambient while being transferred from the aluminum deposition system into the C_{60} deposition system — but long enough for a thin (~10–20 Å) layer of aluminum oxide (Al_2O_3) to grow on the Al down stripes. While this oxide layer is too thin, in comparison with the thickness of the C_{60} film, to affect the bulk capacitance of the structure, it contributes significantly to the interfacial capacitance C_i (see Sec. 3.2.2). In addition, since Al_2O_3 is an excellent insulator, it blocks much of the DC current through the structure, rendering this configuration unusable for transport measurements.[7] Note that, in the context of semiconductor measurements, the bottom interface of the structure shown in Fig. 4-13 would be considered an MIS (metal–insulator–semiconductor) interface. Indeed, the behavior of such an interface in an Al-Al_2O_3-C_{60}-Al "sandwich" structure has been investigated by Yonehara and Pac [129] and others [264], who found such a structure to be strongly

[7]It is instructive to keep in mind the estimate for the resistance expected from a typical trilayer structure similar to that shown in Fig. 4-13. Assuming a typical C_{60} film thickness of 1000 Å and a typical width of 200 μm for both the down stripes and the cross stripes, we calculate that, as the conductivity σ of C_{60} varies from 10^{-7} Ω·cm to 10^{-10} Ω·cm as a result of oxygen exposure, the resistance of the C_{60} layer varies from ~1 MΩ to ~1 GΩ. The resistance of the entire structure will be further increased by the presence of the Al_2O_3 layer at the bottom interface.

rectifying (see Sec. 1.7.3). In the context of the dielectric measurements presented in this work, however, it is sufficient to treat the Al_2O_3 layer[8] as a frequency-independent capacitance C_i in series with the bulk capacitance due to C_{60}.

The microdielectric sensor with interdigitated electrodes (see Figs. 3-6 and 3-10) was utilized for some of the experiments, in which case a C_{60} film of known thickness was deposited directly onto the surface of the sensor.

4.6 Measurement of the intrinsic dielectric constant of C_{60}

In order to ascertain the intrinsic dielectric constant ε' of C_{60}, the dielectric measurement needs to be performed at frequencies low enough to include the intrinsic relaxation processes of the material, but high enough to escape the effect of impurities. We have determined experimentally that the effects of oxygen and other impurities occupying the interstitials of solid C_{60} on the dielectric relaxation of C_{60} films are confined to frequencies below $\sim$5 kHz. A measurement at 100 kHz would thus yield the intrinsic dielectric constant ε' of the material.

Such measurements were performed on trilayer ("sandwich") structures similar to the one shown in Fig. 4-13. Figure 4-14 plots the reciprocal capacitance $1/C$ normalized to the area A of the cross stripes vs film thickness. The linear dependence of the reciprocal capacitance on the film thickness, with finite positive intercept on the ordinate, is consistent with the model described in Sec. 3.2, in which the measured capacitance is equal to the series combination of the interface capacitance and a geometrical capacitance [225]. From the slope of the linear fit through the C_{60} data in Fig. 4-14 (solid circles), a value $\varepsilon' = 4.4 \pm 0.2$ for the relative dielectric constant is

[8]It is important to remember that C_i here includes a contribution due to the Al_2O_3 layer (geometrical), as well as a Al_2O_3-independent component due purely to the interfacial effects discussed in Sec. 3.2.2.

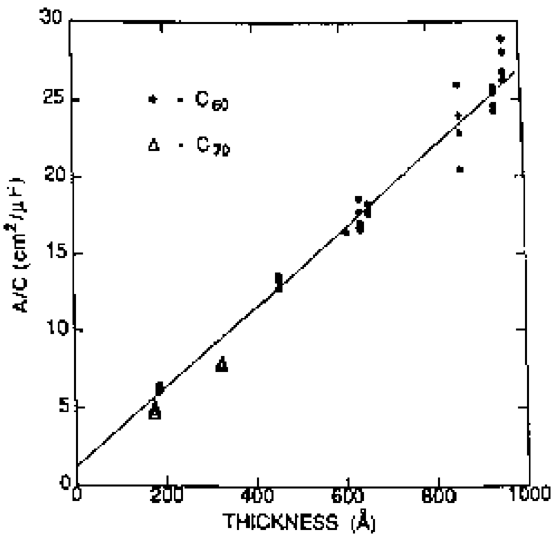

Figure 4-14: Plot of the reciprocal areal capacitance of Al-C_{60}-Al (●) and Al-C_{70}-Al (△) trilayer structures as a function of fullerene film thickness, measured at 100 kHz. A relative permittivity of 4.4±0.2 for C_{60} is calculated from the solid line regression fit to the C_{60} data [24].

calculated. This value is comparable to that of thin-film amorphous SiO_2 which itself is on the low end of the range for thin-film oxide dielectrics [24].

Note that, since the measurements depicted in Fig. 4-14 were performed at 100 kHz, the enhanced polarization effects due to hopping impurities (which make a large contribution to the polarization below 5 kHz) do not interfere with the measurement, and thus the dielectric constant $\varepsilon' \approx 4.4$ is a good approximation of the "true" static dielectric constant of pristine C_{60}. This value is somewhat higher than the value of $\varepsilon' \approx 3.9$ obtained from the optical measurements [61] (see Fig. 4-1.) As noted in Sec. 4.2, this small difference is probably due to the additional losses associated with the rapid molecular rotation motion of C_{60} at room temperature ($T > T_{01}$) and at a frequency of $\sim 10^9$ Hz, as evidenced by NMR [73], ultrasound attenuation [52], and other experiments sensitive to phenomena in this frequency range (see Sec. 1.3.2).

4.7 Dielectric properties as a function of oxygen diffusion

As was discussed above, the interstitial spaces of the fcc C_{60} solid are large enough to accommodate almost any element of the Periodic Table. In this section, we shall investigate how molecular oxygen affects the dielectric properties of C_{60} films (discussion of effects of other species will be deferred to Sec. 4.10). First, we demonstrate that some impurities are present in the lattice by observing nonlinear effects in the dielectric function at low frequencies (Sec. 4.7.1). We then hypothesize that these impurities consist mainly of molecular oxygen, and demonstrate the development of a dielectric loss peak (accompanied by an increase in polarization) with prolonged exposure to ambient oxygen (Sec. 4.7.2). Sec. 4.7.3 demonstrates that very little charge transfer is necessary in order to achieve polarization enhancements reported in Sec. 4.7.2, which makes the oxygen diffusion model of dielectric relaxation in oxygenated C_{60} increasingly plausible. In Sec. 4.7.4, we follow the dielectric loss peak as a function of oxygen content, and propose the model of a *diffusion-controlled relaxation mechanism* for low frequency dielectric relaxation of oxygenated C_{60}, and Sec. 4.7.5 describes how to obtain both tracer and chemical diffusion constants for oxygen diffusion into C_{60} purely from dielectric measurements.

4.7.1 Low-frequency nonlinearities in the dielectric data

In addition to ensuring that the frequency at which the measurement is performed is sufficiently high to avoid impurity contributions to the dielectric function, it is also important to conduct the measurement at voltage levels low enough to avoid nonlinearities, particularly at low frequencies. From the arguments outlined in Sec. 3.2.2, we concluded that a 1000 Å-thick dielectric film measured at 100 mV (corresponding to a field strength of 10^4 V/cm) should stay well within its linear region.

Figure 4-15 displays the real and imaginary parts of the dielectric function of a

500 Å-thick C_{60} film measured at 10 mV (open dots) and 100 mV (solid dots). Clearly, the behavior of the C_{60} film at low frequencies (below ~1 kHz) is *nonlinear*, despite the relatively modest electric field strength of 2×10^4 V/cm. This nonlinearity strongly suggests the presence of weakly bound dipoles in the interstitials of the film. Combining this observation with the evidence from the magnetic studies (Sec. 4.4.1) and transport measurements (Sec. 4.4.2), we hypothesize that these dipoles are created via a charge transfer between the C_{60} balls and the oxygen molecules (O_2) occupying interstitial spaces of the C_{60} lattice. However, the charge transfer may not necessarily be an integral charge, as shown below.

4.7.2 Development of the dielectric loss peaks as a result of oxygen diffusion

The presence of electric dipoles in an oxygenated C_{60} solid is further confirmed by dielectric studies of C_{60} thin films. These studies were performed using either the trilayer sample configuration (shown in Fig. 4-13) for capacitance measurements, or a Micron sensor (Fig. 3-10) using the microdielectrometry technique.

The main feature that shows up consistently in the dielectric measurements of all C_{60} films we have studied is a significant increase in permittivity ε', accompanied by a peak in the dielectric loss ε'', at frequencies on the order of ~100 Hz at room temperature. These features are dependent on both the concentration of oxygen in the interstitials of the film and on temperature. These relationships are investigated in this section and in Sec. 4.8, respectively.

Figure 4-16 displays a representative "snapshot" of the evolution of a 1000 Å C_{60} film after 16 hours of exposure to the ambient environment at room temperature ($T \approx 296°$C). The figure shows the real (a) and imaginary (b) parts of the dielectric function, as well as the loss tangent (c) and the Cole-Cole representation (d). The data for the C_{60} film (solid lines) are compared to the Debye single-relaxation-time model (see Sec. 2.3.3) described by Equations (2.46) and (2.47). We notice right away that

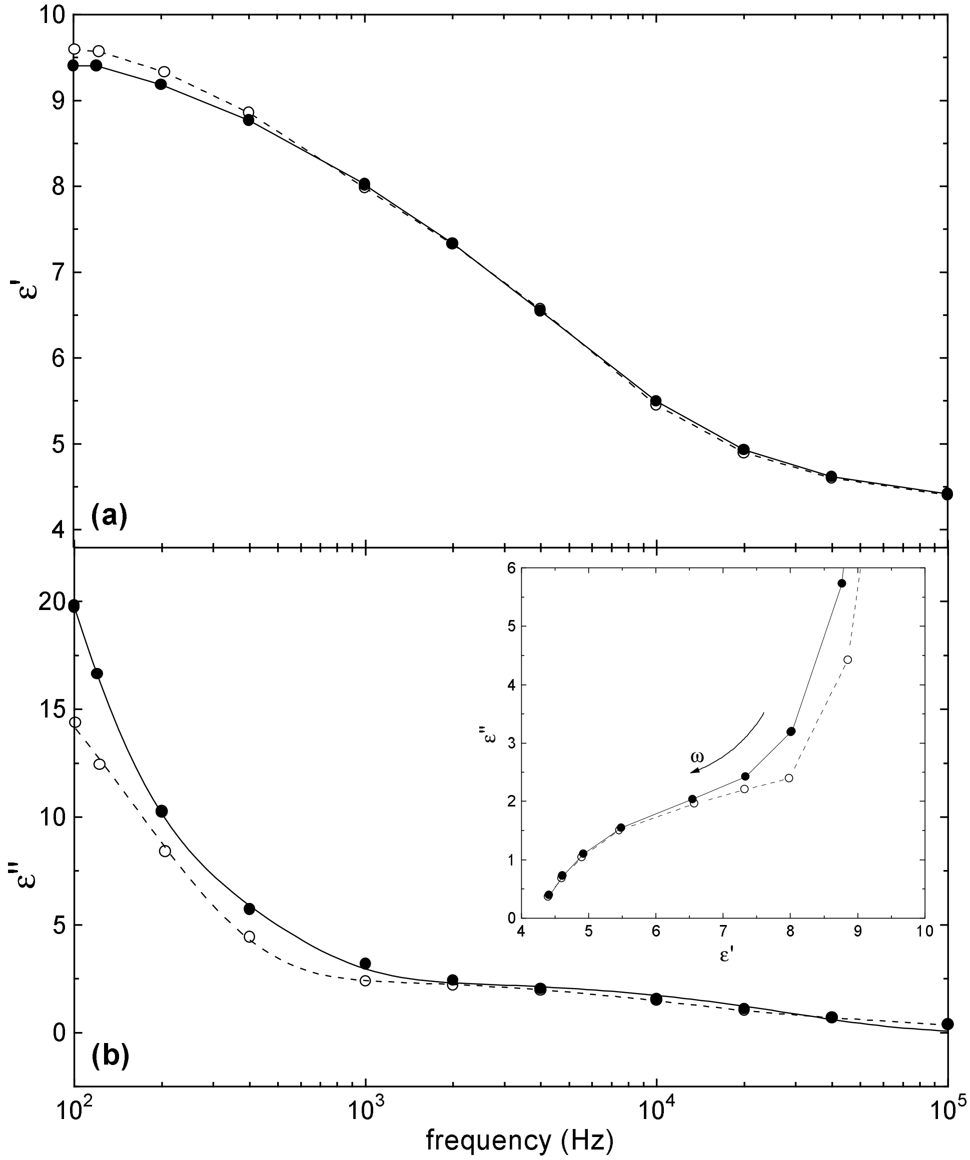

Figure 4-15: Evidence of nonlinear behavior of a C_{60} film at low frequencies (below ~1 kHz) due to the presence of weakly bound dipoles. A 500 Å-thick C_{60} film was measured at 10 mV excitation (○, dashed lines) and 100 mV excitation (●, solid lines). The real (a) and imaginary (b) parts of the dielectric function are displayed. The inset shows the Cole-Cole plot of the sample, with the arrow indicating the direction of the frequency increase. The shape of the Cole-Cole plot suggests a Debye-like dielectric relaxation mechanism combined with a DC conductivity effect (see Fig. 2-20).

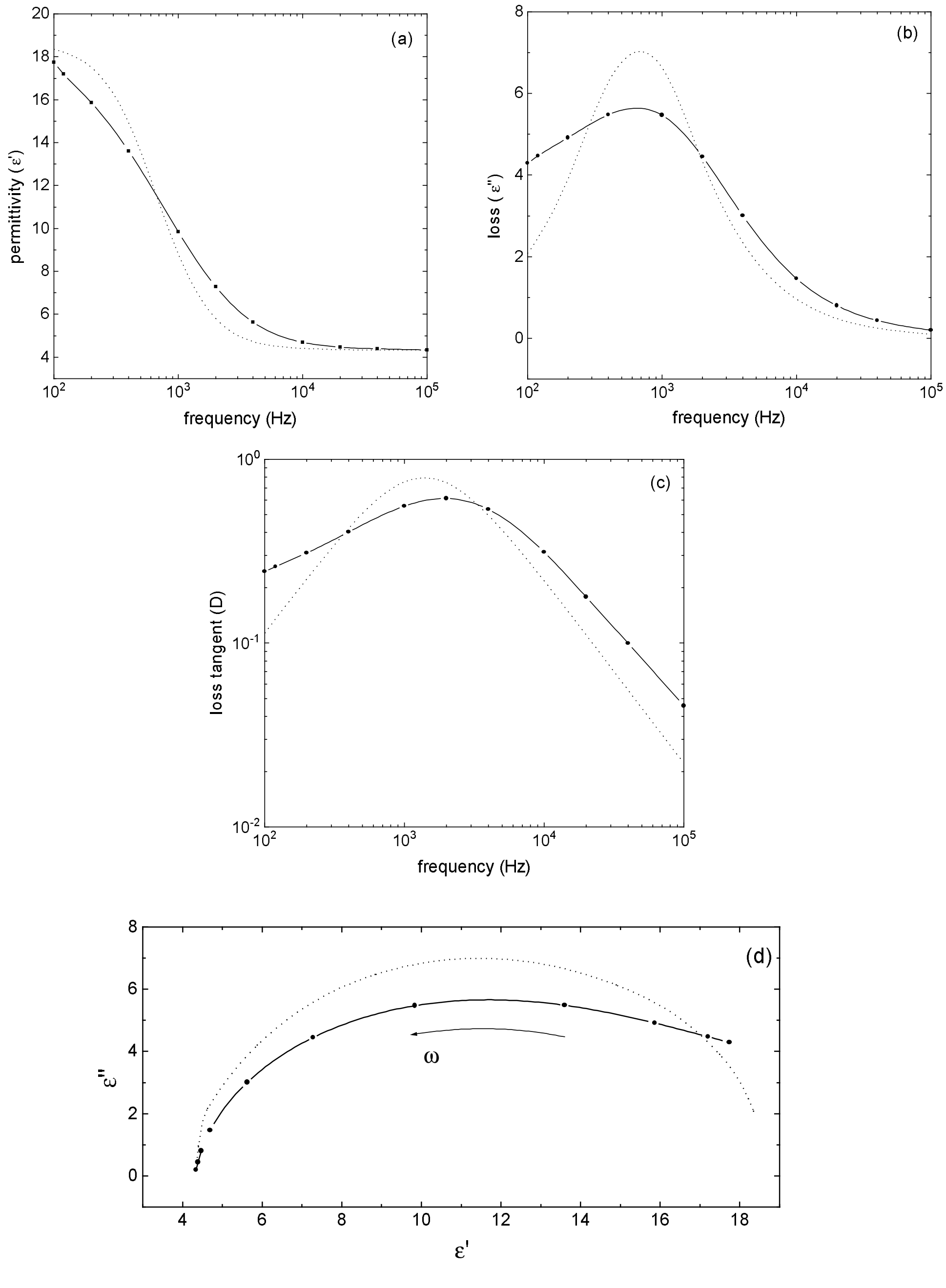

Figure 4-16: Dielectric response of a 1000 Å C_{60} film after 16 hours of exposure to the ambient environment at room temperature ($T \approx 296°C$). The real (a) and imaginary (b) parts of the dielectric function are plotted on a log-linear scale, whereas the loss tangent (c) is shown on a log-log scale. Plot (d) displays the Cole-Cole representation of the data. The dotted lines correspond to the Debye relaxation function [Equations (2.45)] with the following parameters: $\varepsilon_\infty = 4.34$, $\varepsilon(0) = 18.66$, $f_{\text{peak}} = 674\,\text{Hz}$, $\tau_d = 1/2\pi f_{\text{peak}} = 236\mu\text{s}$.

our system cannot be adequately described by a simple Debye relaxation mechanism. The linear fits to the log-log plot of the loss tangent data in Fig. 4-16(c) suggest the high-frequency and low-frequency exponents of 0.87 and 0.19, respectively. Referring to Table 2.2, we discover that no single-parameter models (Cole-Cole, Davidson-Cole, or Williams-Watts) are able to fit the data. We shall, therefore, utilize Jonscher's "many-body interactions" approach leading to the two-parameter model of dielectric relaxation [177] described in Sec. 2.3.3.

4.7.3 Calculation of added polarization

The development of the dielectric peaks, such as the one shown in Fig. 4-16, after oxygen exposure provides further evidence of the presence of dipoles in oxygenated C_{60} films. The fact that both C_{60} and molecular oxygen (O_2) molecules are non-polar, together with the evidence for reversible oxygen diffusion into the bulk of C_{60} solid (Sec. 4.4.1-4.4.2), strongly suggests that these dipoles arise due to a charge transfer between oxygen molecules and C_{60} balls. On the other hand, the amount of this charge transfer is bound to be very small, reflecting the fact that the electron affinities of both C_{60} and molecular oxygen are relatively high. The direction of charge transfer can be ascertained by comparing the electron affinities of these two molecules. Since the electron affinity of C_{60} molecule (2.65 ± 0.05 eV [40]) is considerably higher than the electron affinity of molecular oxygen (0.451 ± 0.007 eV [265]), we expect oxygen to be the donor and C_{60} the acceptor of electrons.[9]

Even though the amount of charge transferred from an oxygen molecule to a C_{60} molecule may be small, it can create a relatively large effective dipole moment if the charge is transferred over a large distance. To calculate the amount of charge that needs to be transferred in order to achieve the added polarization evident in

[9] One should be careful when using the values for electron affinity for making prediction regarding the direction of charge transfer, as these numbers are modified by the lattice screening effects in the solid. In the case of C_{60}, these are good estimates, however, because C_{60} forms a loosely bound *molecular* solid (Sec. 1.3.2).

Fig. 4-16(a), we shall use the Clausius-Mossotti equation (2.11). As discussed in Section 2.2.3, the relative permittivity ε' of a solid is linked to the dipole moment μ of the permanent dipoles contained in the solid and to the molecular polarizability α_m via the Clausius-Mossotti formula

$$\frac{\varepsilon' - 1}{\varepsilon' + 2} = \frac{N_d \mu^2}{9\varepsilon_0 kT} + \frac{4\pi N_m \alpha_m}{3}, \tag{4.6}$$

where N_m is molecular density of the solid, N_d is the density of permanent dipoles, T is temperature, and the fundamental constants are $\varepsilon_0 = 8.85 \times 10^{-12}\,\mathrm{F/m}$ and $k = 1.38 \times 10^{-23}\,\mathrm{J/K}$, the permittivity of free space and the Boltzmann constant, respectively. In the absence of permanent dipoles, the molecular polarizability is, therefore,

$$\alpha_m = \frac{3}{4\pi N_m} \frac{\varepsilon' - 1}{\varepsilon' + 2}. \tag{4.7}$$

Setting $\varepsilon = 4.4$ and $N = 1.44 \times 10^{21}\,\mathrm{cm}^{-3}$ (molecular density for C_{60} solid), we get $\alpha_m = 90\,\text{Å}^3$ for the polarizability at $\omega = 10^5\,\mathrm{Hz}$. This value compares well with other determinations of the low-frequency molecular polarizability of C_{60} [235, 266–268].

We explain the dramatic increase in the dielectric function $\varepsilon'(\omega)$ from 4.4 at 10^5 Hz to 18.4 at 100 Hz by polarization caused by the interstitial oxygen. We determine the strength μ of a permanent dipole at room temperature by solving equation (4.6) with $\varepsilon = 18.4$, $\alpha_m = 90\,\text{Å}^3$, and $T = 300\,\mathrm{K}$, which yields $\mu \approx 0.9$ Debye. We then represent each C_{60} molecule as a conducting sphere of radius $R \approx 5\,\text{Å}$, and each oxygen molecule as a point-charge q transferring a fractional charge onto the C_{60} molecule (Fig. 4-17). From an image charge calculation, we obtain the dipole moment

$$\mu = -qa\left[1 - \left(\frac{R}{a}\right)^3\right] \tag{4.8}$$

created by the transfer of a charge q onto a sphere of radius R located distance a away from the charge q (see Fig. 4-17). For the C_{60} solid with O_2 in the octahedral

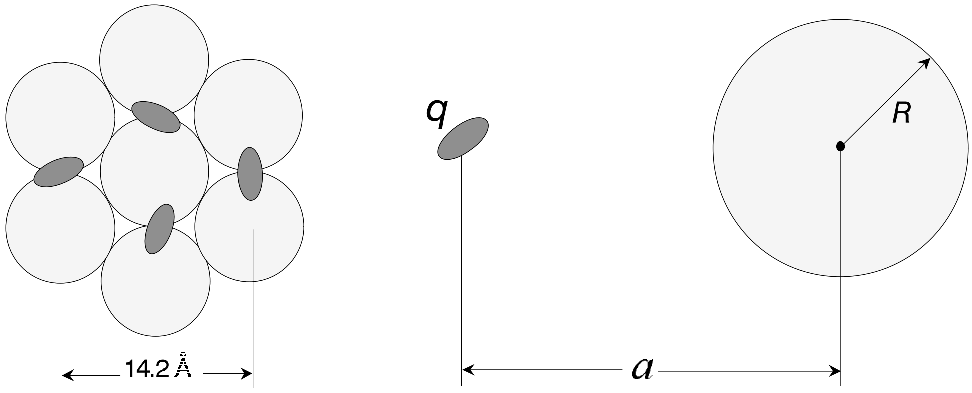

Figure 4-17: A schematic drawing (2D projection) showing oxygen molecules (represented by ellipses) located in the interstitials of the C_{60} solid (with buckyballs represented by spheres). The fcc C_{60} lattice constant is 14.2 Å. The figure to the right is used in the image charge calculation to obtain Eqn. (4.8) for the dipole moment. The reader should refer to Fig. 4-2 for a more realistic rendition of the three-dimensional C_{60}/O_2 compound.

sites, $R \approx 5\,\text{Å}$ and $a \approx 7\,\text{Å}$, and so q is determined to be

$$q \sim 0.04 q_{\bar{e}},$$

where $q_{\bar{e}} = 1.6 \times 10^{-19}$ Coulomb is the elementary charge on an electron. Clearly, it is very plausible to expect this small amount of charge transfer to occur between a C_{60} molecule and an interstitial oxygen molecule through a hybridization mechanism.[10] This validates our assumption[11] regarding the origin of the dipoles in oxygenated C_{60}.

[10]Note that this calculation ignores the contribution from other C_{60} molecules surrounding a particular oxygen molecule (see Fig. 4-17). The dipole moment μ will only arise if the oxygen molecule is displaced from the center of the interstitial site.

[11]See Sec. 4.7.6 for a discussion of other plausible dipole-forming mechanisms related to various interface effects.

4.7.4 Dynamics of the dielectric loss peaks as a function of oxygen diffusion

In one of the most fascinating results of our studies of low-frequency dielectric properties of C_{60} films, we found that the dielectric loss peaks described above (see Fig. 4-16 in Sec. 4.7.2) change their magnitude, shape, and frequency position as a function of oxygen diffusion onto the bulk of the film. Figure 4-18 illustrates schematically the dynamics of the loss peak as a function of exposure to ambient oxygen. The top trace in Fig. 4-18 shows that as-prepared films display very little anomalous dielectric dispersion, resulting in the absence of the dielectric loss peak. The $1/\omega$ rise in the dielectric loss toward low frequencies is due to the finite DC conductivity of the sample, as discussed in Sec. 2.3.4. With prolonged exposure to oxygen, the dielectric loss peak becomes more pronounced, and gradually moves towards higher frequencies by about an order of magnitude (middle traces in Fig. 4-18). With additional exposure, however, the dielectric loss peak decreases again, until it finally disappears completely after about two weeks of exposure. After heat treatment in vacuum, the dielectric peak reappears, as illustrated by the bottom trace in Fig. 4-18.

We explain the dynamics of the dielectric loss peak in terms of the oxygen diffusion and O_2-C_{60} charge transfer models described in Sec. 4.7.3 above. Since no oxygen is present in the as-prepared C_{60} film (top trace in Fig. 4-18), no charge transfer occurs, and thus no dipoles are present. Therefore, no anomalous dielectric dispersion occurs in the material.

Once the sample is placed in the ambient environment, molecular oxygen starts diffusing into the bulk of the film, transferring charge to the neighboring C_{60} balls, and thus creating electrical dipoles, as described in Sec. 4.7.3. As the oxygen molecule diffuses through the C_{60} lattice, it "drags" this transferred charge from one C_{60} ball to the next along its path. Thus diffusion of an oxygen molecule through the lattice, which, on the microscopic level, is a random walk-like process (see Sec. 4.7.5), has the effect of flipping the O_2-C_{60} dipoles at some rate determined by the oxygen diffusion

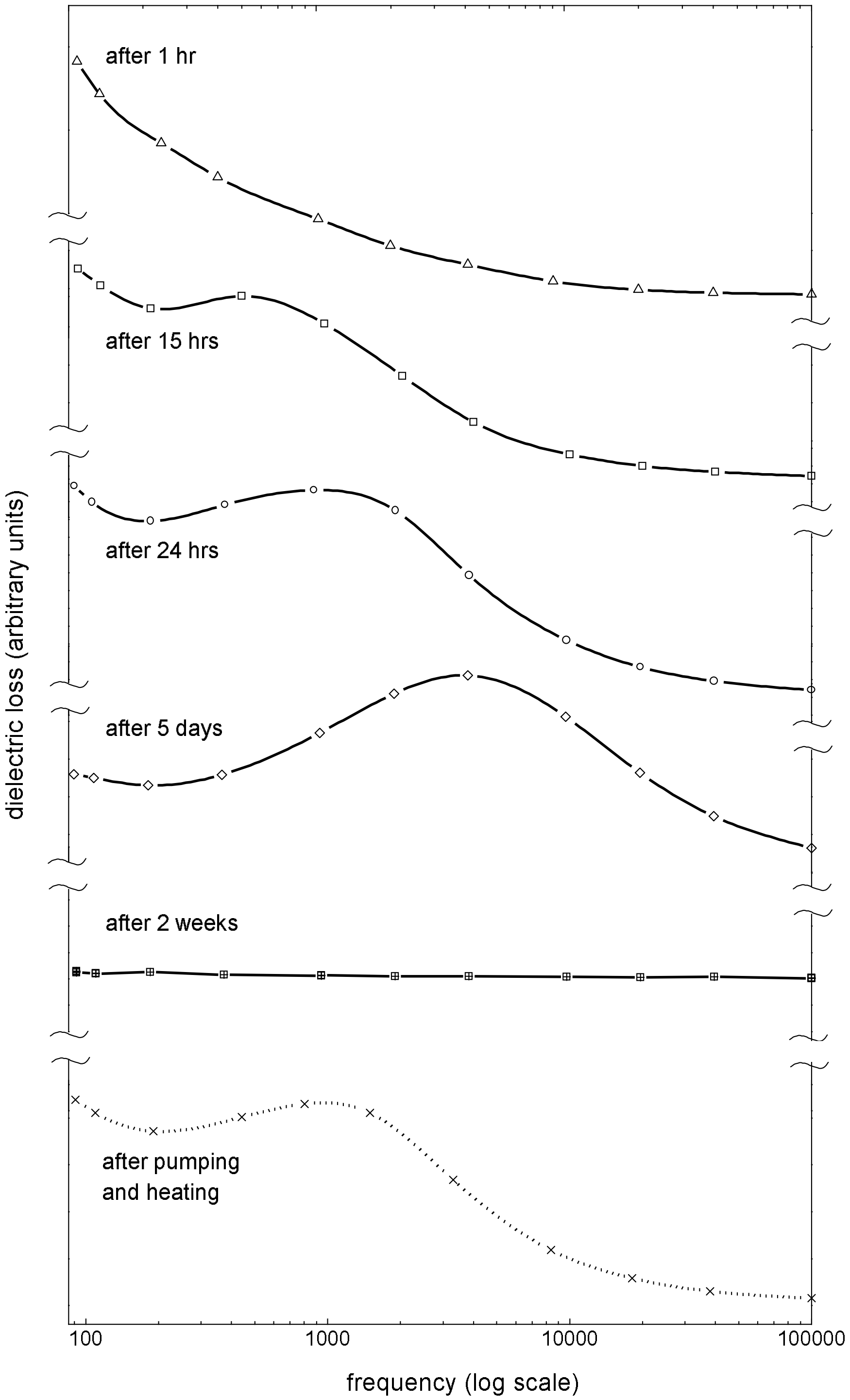

Figure 4-18: A schematic plot of dielectric loss vs frequency for a 1000 Å C_{60} film, prepared initially without exposure to oxygen, showing peaks moving after various durations of oxygen exposure. The y-axis scale is the same for all traces. The traces have been stacked vertically for clarity.

constant and the hopping distance. An applied AC electric field can couple to this process, yielding a loss peak at some frequency determined by the rate of oxygen hopping, which, in turn, is controlled by the diffusion constant of oxygen in its C_{60} host.

We, therefore, propose a *diffusion-controlled relaxation* mechanism for low frequency dielectric relaxation in oxygenated C_{60}.

In the pristine C_{60} film, in the absence of a charge-transferring diffusant (such as O_2), no enhanced polarization [Fig. 4-19(a)] or anomalous dielectric dispersion [Fig. 4-19(b)] is observed. As a greater fraction of the interstitial sites gets filled by diffusion, more dipoles are created via charge transfer, which results in increased polarization and the development of a dielectric loss peak at the characteristic hopping frequency of the molecules. As the number of empty sites decreases, oxygen molecules may need to hop to the second nearest neighbor sites, which requires more energy, and is therefore much less likely to occur, resulting in a decrease in the additional polarization and in the magnitude of the loss peak. With increasing oxygenation, a nearly full occupancy of the interstitial sites is eventually achieved, interstitial hopping is inhibited, and the loss peaks, together with the enhanced polarization, disappear.

To exclude the possibility that the observed enhanced polarization behavior is due to some kind of an electrode effect, we also manufactured trilayer structures qualitatively similar to those in Fig. 4-13, but with the electrodes made of metals other than aluminum (Ag, Au, Cr). A representative result of dielectric measurements performed on a Al-C_{60}-Ag trilayer structure is shown in Fig. 4-20. Clearly, this result is similar to those obtained with Al-C_{60}-Al trilayers. We tentatively conclude that the enhanced polarization effects that we observe are due to intrinsic properties of the C_{60}-O_2 system, and not to the electrode effects.[12]

[12] A thickness dependence study with Al-C_{60}-Al trilayers is needed to further clarify the significance of electrode effects. By varying the thickness of the C_{60} layer, it should be possible to reliably isolate bulk C_{60} properties from the interface effects. Preparations for such a study are currently under way. See Sec. 4.7.6 for additional discussion of possible interface-related sources of polarization in this system.

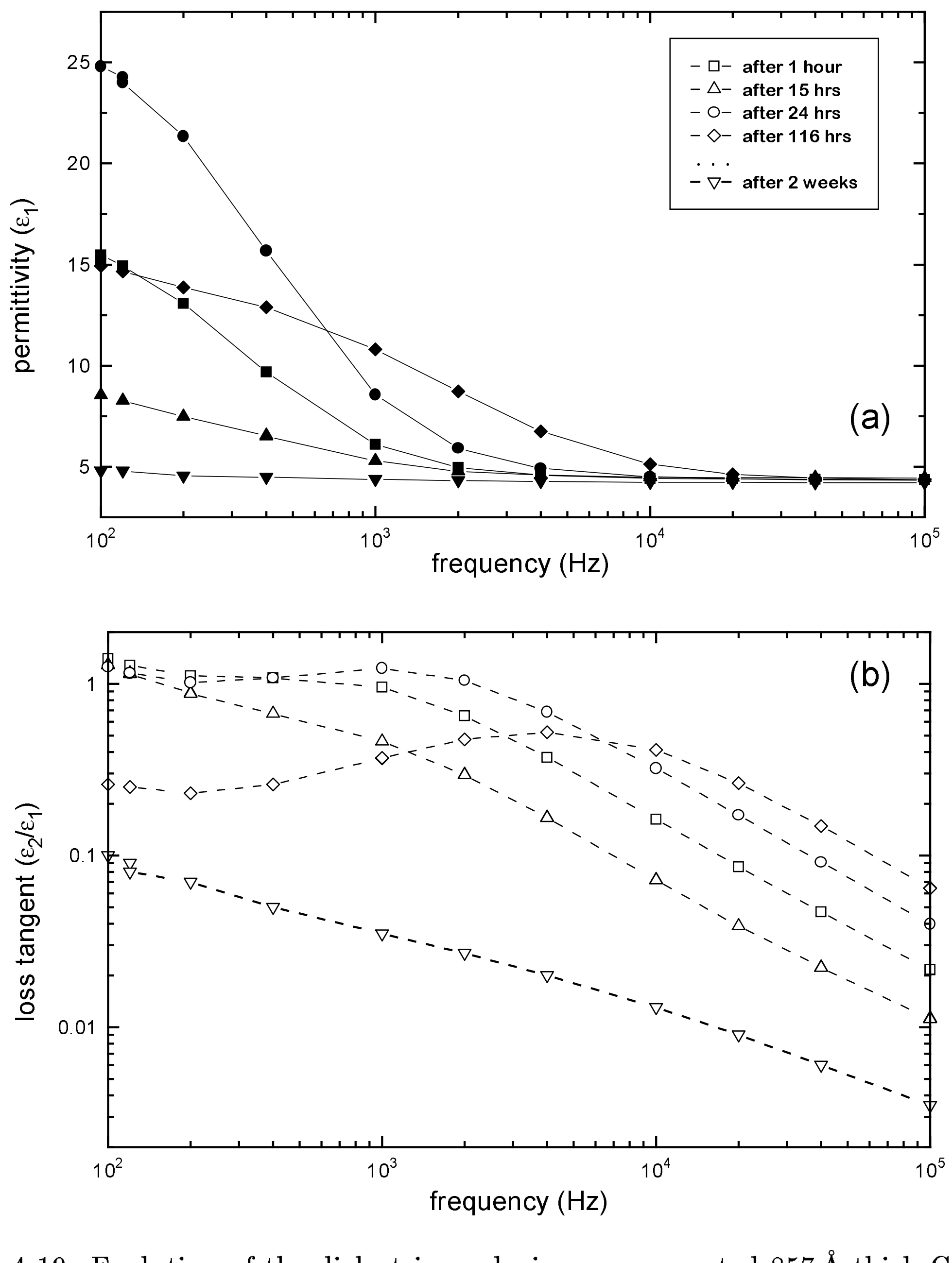

Figure 4-19: Evolution of the dielectric peaks in an oxygenated 857 Å-thick C_{60} film with exposure to the ambient atmosphere. Note that, while the permittivity is plotted on a log-linear scale (a), the dielectric loss tangent is plotted on a log-log scale (b).

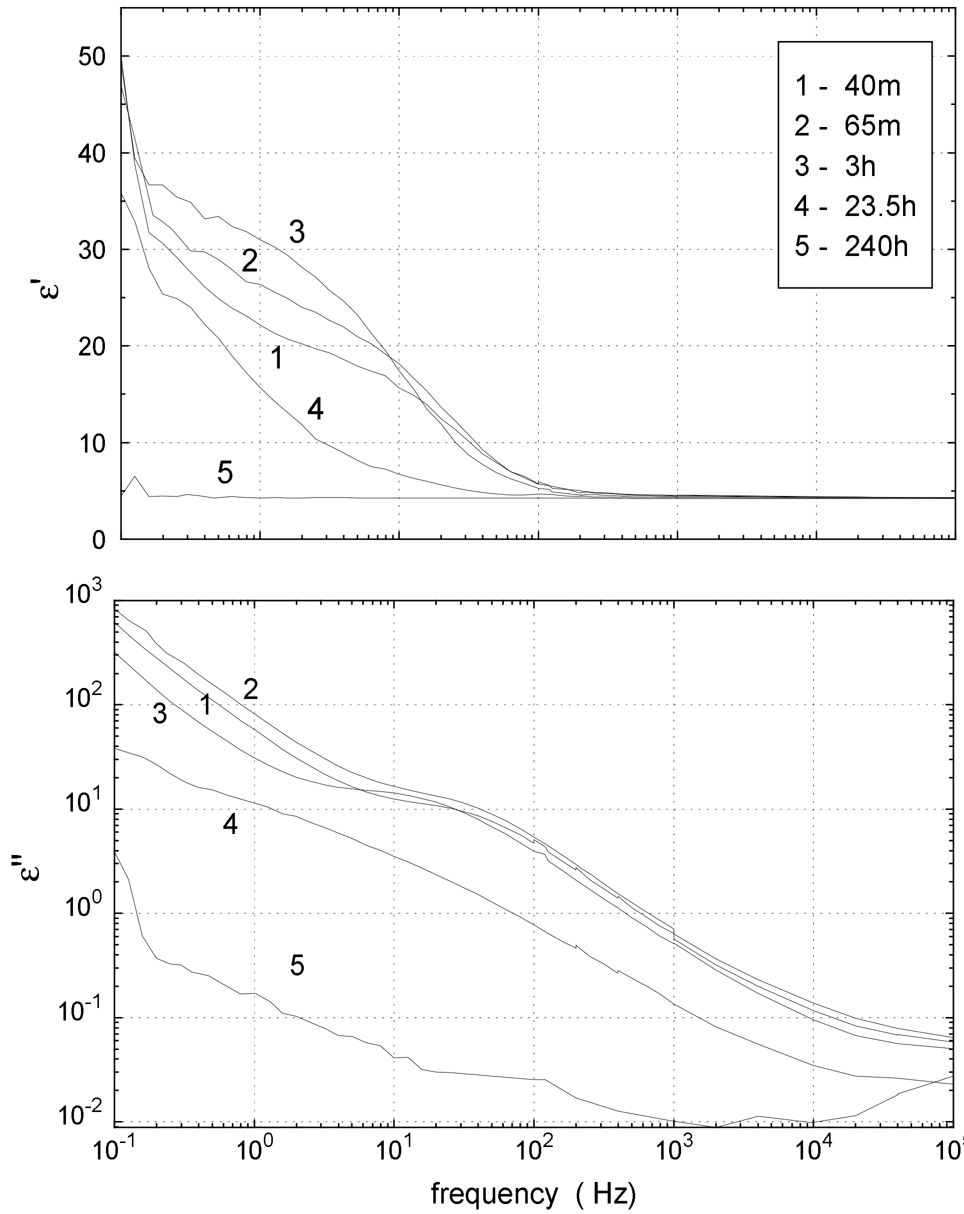

Figure 4-20: Enhanced polarization and anomalous dispersion effects observed in a Al-C_{60}(650Å)-Ag trilayer structure. Note that the data were taken over an extended frequency range, compared to that of Fig. 4-19.

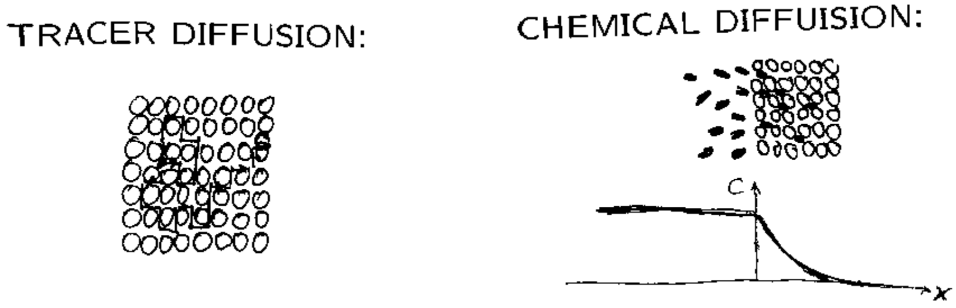

Figure 4-21: Illustration of the tracer and chemical diffusion processes in two dimensions. The hollow circles represent atoms or molecules of the host material arranged in a regular lattice, into which the diffusant is diffusing. Tracer diffusion is a random walk-like process. The graph for the case of chemical diffusion shows a snapshot concentration of the material as a function of position x at some time t. The concentration of the diffusant outside the sample is constant, and it decreases with x into the bulk of the material.

4.7.5 Obtaining the chemical and tracer diffusion constants from the dielectric loss data

There are two different diffusion constants that are important in thermodynamics: a tracer diffusion constant, D_{tracer}, and a chemical diffusion constant, D_{chem} (the latter usually being simply designated as D)[13]. To our knowledge, both of them have never been obtained at the same time using dielectric measurements either on C_{60} or on any other material. Our dielectric measurement techniques (see Chapter 3), spanning nine orders of magnitude in frequency, allowed us to obtain both of the constants simultaneously for the C_{60}-O_2 system.

The tracer and chemical diffusion processes are illustrated in Fig. 4-21. Tracer diffusion is usually described as a random walk of the diffusing species (diffusant)

[13]Both D_{tracer} and D_{chem} can vary with temperature, concentration, and other factors, so it would be more precise to call them diffusion *coefficients,* rather than *constants.* The name *diffusion constant* is still often used, however, implying the diffusion coefficient measured at some assumed point in the phase space (usually, at room temperature, with diffusion coefficient presumed to be concentration-independent, unless noted otherwise).

in the lattice of the host material. The tracer diffusion constant is defined by the *Einstein relation:*

$$D_{\mathrm{tracer}} = \frac{\langle d^2 \rangle}{2\tau}, \tag{4.9}$$

where d is the average hopping distance, and τ represents the time required for a single *hop* in the random walk chain.

The chemical diffusion constant D_{chem} describes the distribution of a diffusant in the host material. D_{chem} can be thought of as a *macroscopic* diffusion constant, and it relates to the *microscopic* tracer diffusion constant D_{tracer} via the following equation

$$D_{\mathrm{chem}} = F D_{\mathrm{tracer}} \tag{4.10}$$

where

$$F = \frac{C}{k_B T} \frac{\partial \mu}{\partial C}, \tag{4.11}$$

C is composition (in number of particles per volume), μ is the chemical potential, T is the temperature, and $k_B = 1.38 \times 10^{-23}$ J/K is the Boltzmann constant.

The distribution of a diffusant in a given film during absorption (or desorption) is governed by the one-dimensional differential equation for diffusion due to Fick [269] (Fick's First Law), with the space coordinate x taken in the direction of the film thickness (see Fig. 4-21):

$$\frac{\partial C(x,t)}{\partial t} = -\frac{\partial J}{\partial x}, \tag{4.12}$$

where $C(x,t)$ is the concentration and J is the flux of the diffusant. For a description of nonsteady-state problems, it is necessary to combine Fick's first law (4.12) with a differential mass balance equation stating that a change in the diffusant's concentration $C(x)$ results in a flux $J(x)$:

$$J = -D\frac{\partial C}{\partial x} \tag{4.13}$$

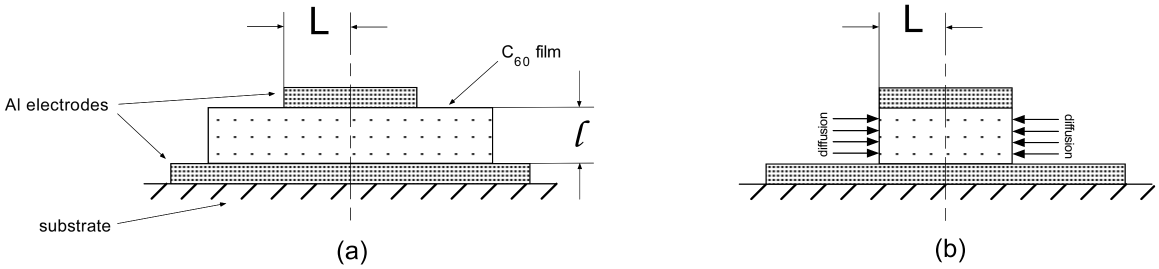

Figure 4-22: (a) A single M-C_{60}-M (M=metal) junction similar to those shown in Fig. 4-13, where ℓ represents the thickness of the C_{60} film, and L is one half of the electrode width. (b) An approximation used in deriving Eqns. (4.15) and (4.16) assumes that the initial concentration is equal to C_1 across the C_{60} film's edges. This approximation requires that $\ell \ll L$. For typical values of $\ell \sim 1000\,\text{Å}$ and $L \sim 100\,\mu$m, this requirement is clearly fulfilled, and the use of this approximation is justified.

where D is the (chemical) diffusion coefficient. Combining Eqns. (4.12) and (4.13), we arrive at Fick's Second Law:

$$\frac{\partial C(x,t)}{\partial t} = D\frac{\partial C^2}{\partial^2 x} + \frac{\partial D}{\partial C}\left(\frac{\partial C}{\partial x}\right)^2, \tag{4.14}$$

where we allowed for the possibility that the diffusion coefficient D is a function of concentration C.

Solutions of Fick's second law (4.14) for various geometries and initial conditions have been compiled by Crank [270]. For the case of lateral diffusion into the film of the kind expected in our Al-C_{60}-Al trilayer structures (see Fig. 4-13), the concentration of diffusant (*e.g.*, molecular oxygen) at distance x into the film after time t is found as [270]

$$\frac{C(x,t) - C_0}{C_1 - C_0} = 1 - \frac{4}{\pi}\sum_{n=0}^{\infty}\frac{(-1)^n}{2n+1}\cos(\alpha_n x)e^{-D\alpha_n^2 x} \tag{4.15}$$

where C_0 is the initial concentration of the diffusant in the film (zero), C_1 is the concentration at surface (saturated), D is the diffusion coefficient, $\alpha_n = \frac{(2n+1)\pi}{2L}$, and L is equal to one half of the electrode width (see Fig. 4-22). Figure 4-23 presents a plot of $C(x,t)$ as a function of t for several values of x (top), and a plot of $C(x,t)$ as a function of x for several values of t (bottom). Together, these plots demonstrate that, as $t \to \infty$, the diffusant concentration becomes the same (uniform) throughout the film. (Note also that n only need to be carried to about $n_{\max} = 20$ for convergence of the summation.)

If $M(t)$ denotes the total amount of diffusing substance which has entered the film at time t, and M_∞ is the amount at equilibrium ($t \to \infty$), then the solution to Fick's second law can be written as [270]

$$\frac{M(t)}{M_\infty} = 1 - \frac{8}{\pi^2} \sum_{n=0}^{\infty} \frac{1}{(2n+1)^2} \exp\left[-D(2m+1)^2 \pi^2 \frac{t}{4L^2}\right]. \tag{4.16}$$

The value of t/L^2 for which $M(t)/M_\infty = \frac{1}{2}$, conveniently written as $t_{1/2}/L^2$, is given approximately by

$$\frac{t_{1/2}}{L^2} = -\frac{1}{\pi^2 D} \ln\left[\frac{\pi^2}{16} - \frac{1}{9}\left(\frac{\pi^2}{16}\right)^9\right], \tag{4.17}$$

the error being about 0.001% for typical values of the parameters [271]. Thus the approximation

$$D = 0.04919 \left(\frac{L^2}{t_{1/2}}\right) \tag{4.18}$$

can be used so that if the half-time of the sorption process $t_{1/2}$ is observed experimentally, the value of the diffusion coefficient, assumed constant, can be determined.

In a remarkable illustration of the power and usefulness of dielectric measurements, we were able to measure both the tracer and chemical diffusion constants of oxygen in C_{60} in a single measurement. Figure 4-24 displays the results of this measurement, plotting both the real $\varepsilon'(\omega)$ and imaginary $\varepsilon''(\omega)$ parts of the dielectric function over a broad frequency range. The measurement was performed on a 1000 Å-thick C_{60} film in the "sandwich" configuration (see Fig. 4-13). To map the dielectric function over nine decades in frequency, we had to utilize both the HP 4274A LCZ meter (for measurements from 100 Hz to 100 kHz) and the SI 1254 Frequency Response Analyzer (for measurements below 30 Hz), in configurations described in Sec. 3.2.3.

$n_{max} := 20 \qquad D := 1 \qquad L := 1 \qquad C_0 := 0 \qquad C_1 := 1$

Solution of the Fick's law: $\alpha(n) := \dfrac{(2\cdot n+1)\cdot\pi}{2\cdot L}$

$$C(x,t) := C_0 + \left(C_1 - C_0\right)\cdot\left[1 - \frac{4}{\pi}\cdot\sum_{n=0}^{n_{max}} \frac{(-1)^n}{2\cdot n - 1}\cdot\exp\left(-D\cdot\alpha(n)^2\cdot t\right)\cdot\cos(\alpha(n)\cdot x)\right]$$

$t := 0, 0.01 .. 1$

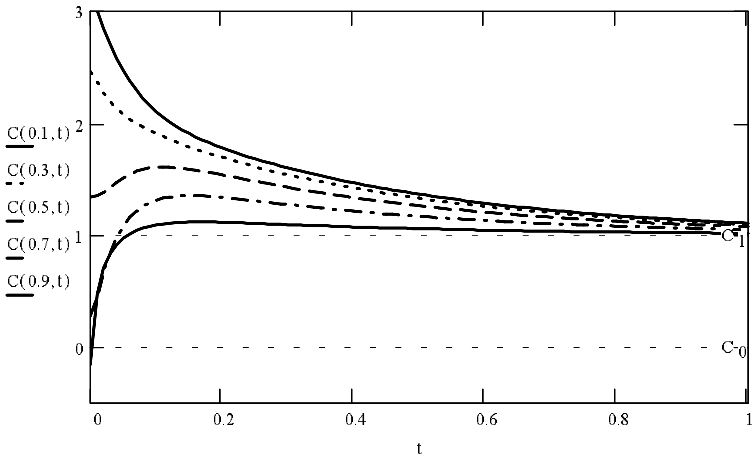

$x := 0, 0.01 .. 1$

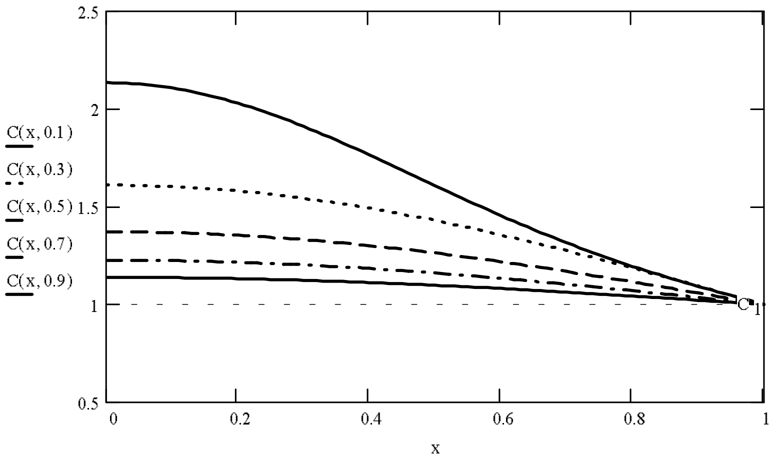

Figure 4-23: Mathcad worksheet calculating Fick's law solutions for the concentration $C(x,t)$ as a function of time t (top plot) and coordinate x (bottom plot).

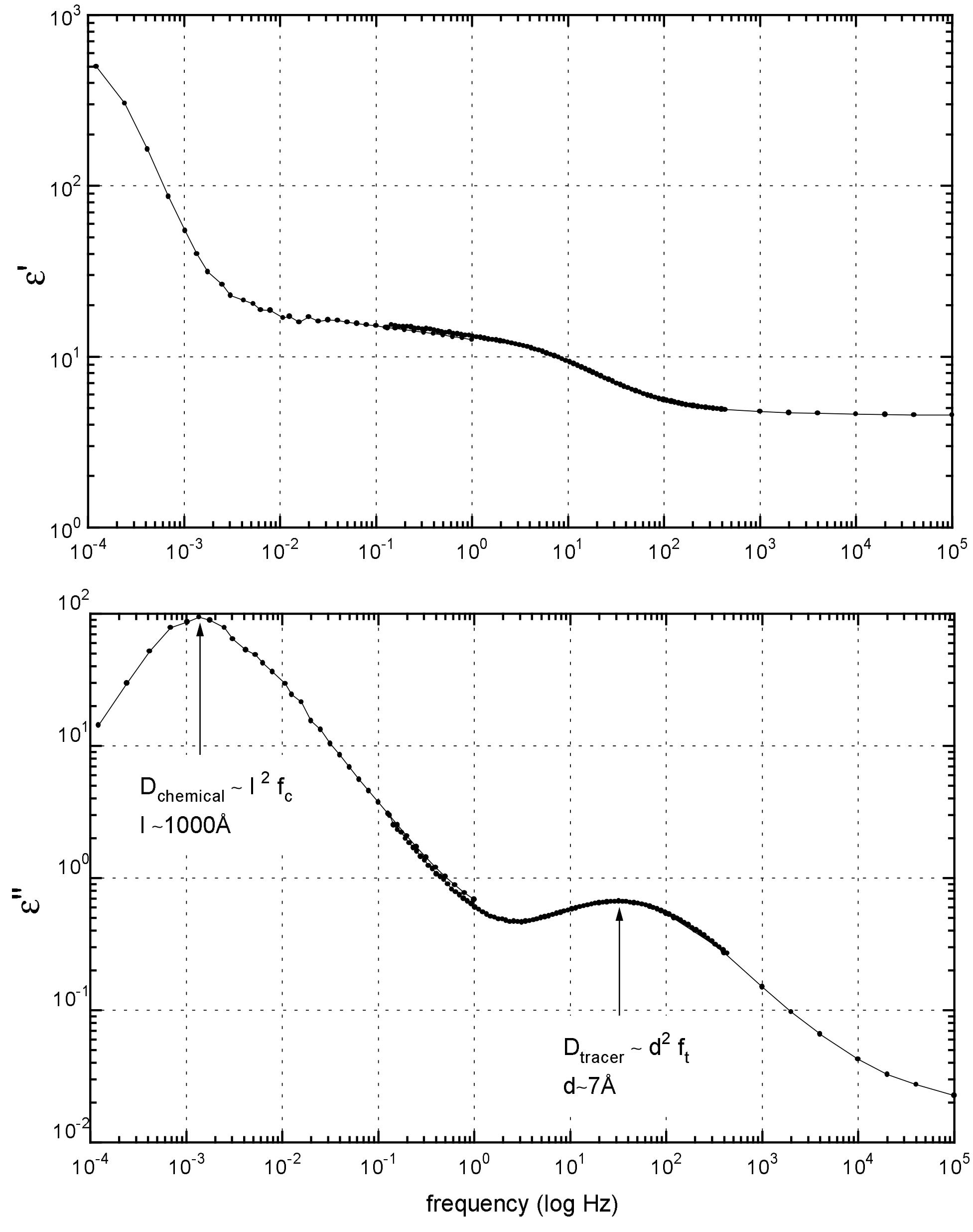

Figure 4-24: Plot of $\varepsilon'(\omega)$ and $\varepsilon''(\omega)$ used to determine the molecular oxygen diffusion into a C_{60} film. Both tracer and chemical diffusion processes are indicated.

An additional preamplifier stage was necessary for measurements below 1 Hz, due to the increased effective conductivity of the sample at low frequencies. The excellent overlap of the data in the three measurement regions confirms the validity of our measurement technique.

In addition, the DC resistance has been subtracted from the dielectric data, as described in Sec. 2.3.4. Therefore, only dielectric polarization and loss, not obscured by the DC conductivity, are shown in Fig. 4-24.

The Einstein relation [Eqn. (4.9)] can be written in the frequency domain as

$$D_{\text{tracer}} = \frac{1}{2}\langle d\rangle^2 f_t, \tag{4.19}$$

where $\langle d\rangle \approx 7$ Å is the average oxygen molecule hopping length corresponding to the distance between two neighboring octahedral sites (see Figs. 4-17 and 4-2), and $f_t = 1/\tau \approx 35$ Hz is the hopping frequency determined from the position of the dielectric loss peak in Fig. 4-24. The tracer diffusion constant can thus be determined from Eqn. (4.19) as

$$D_{\text{tracer}} \approx 10^{-13}\text{cm}^2 \cdot \text{sec}^{-1}.$$

To find the chemical diffusion coefficient D_{chem}, we first refer to Fig. 4-19 following the evolution of the polarization and dielectric loss as a function of oxygen diffusion. As is evident from the figure, both polarization and loss achieve their maximum positions after $\sim$24 hrs of exposure to the ambient environment, corresponding to half-occupancy of the sites that are eventually occupied by oxygen, as described in Sec. 4.7.4. This gives $t_{1/2} \sim 24$ hrs for the half-time of the sorption process of Eqn. (4.18).

On the other hand, the same diffusion process that leads to the development and subsequent disappearance of the tracer diffusion (molecular hopping) dielectric loss peak in Fig. 4-19, should also show up as a "relaxation" of the interfacial polarization in the dielectric measurements. We can thus extend Eqn. (4.18) to incorporate the chemical diffusion values obtained from dielectric measurements (Fig. 4-24):

$$D \approx 0.05 \left(\frac{L^2}{t_{1/2}} \right) \approx \ell^2 f_c, \tag{4.20}$$

where f_c is the frequency position of the chemical diffusion-related loss peak in Fig. 4-24, corresponding to millihertz frequencies. The origins of the chemical diffusion-related apparent polarization increase and the accompanying loss peak in Fig. 4-24 should be attributed to the interfacial polarization due to oxygen ions drifting back and forth between the plates of the capacitor under the applied very-low-frequency electric field. We estimate the chemical diffusion of molecular oxygen in C_{60} at room temperature as

$$D_{\text{chem}} \approx 10^{-14}\text{cm}^2 \cdot \text{sec}^{-1},$$

approximately an order of magnitude lower than the tracer diffusion constant.

We have, therefore, demonstrated that the chemical diffusion constant can be determined by dielectric measurements either by following the evolution of the *tracer* diffusion (hopping) loss peak and detecting the half-time of the sorption process $t_{1/2}$, or by direct measurement of $f \sim 1/t_{1/2}$ via detecting the dielectric loss peak at very low frequencies due to *interfacial* polarization.

4.7.6 Alternative dipole-forming mechanisms

The oxygen-induced charge transfer mechanism presented above explains very well the main features of the dielectric behavior of C_{60} films that we observe:

1. development of a low frequency polarization increase accompanied by a dielectric loss peak;
2. evolution of this loss peak with increasing oxygen content; and
3. eventual disappearance of the loss peak and additional polarization with full oxygenation of the specimen (once the majority of the interstitial lattice sites

is occupied).

In addition, there is ample evidence to support the proposition that oxygen does indeed diffuse into the interstitials of a fullerite (see Sections 4.4.1 and 4.4.2).

Still, it would not be prudent to neglect mentioning other possible sources of additional polarization that would cause the films to exhibit similar dielectric behavior.

One such effect relates to the interaction of C_{60} with the top and bottom Al interfaces in an Al-C_{60}-Al trilayer structure, such as those used in our dielectric measurements. Diffusion of Al atoms during and after the deposition of the top electrode is of particular concern, since charge transfer between an Al atom and a C_{60} molecule may be quite considerable, resulting in a large additional polarization. While no definitive study of Al-C_{60} surface interaction has been conducted to date, there are indications that strong surface interaction, with possible formation of surface dipoles, does exist:

- Using Auger electron spectroscopy (AES) and temperature-programmed desorption (TPD), Hamza *et al.* [272] demonstrated that a monolayer coverage of C_{60} passivates aluminum surfaces, preventing formation of aluminum oxide after exposure to oxygen and water vapor from room temperature up to 600 K.

- As mentioned in Sec. 4.5, the behavior of Al-C_{60} interfaces in an Al-Al_2O_3-C_{60}-Al "sandwich" structure has been investigated by Yonehara and Pac [129] and others [264], who found such an MIS (metal–insulator–semiconductor) structure to be strongly rectifying (see Sec. 1.7.3).

- By studying $\{\text{Al-C}_{60}\}_n$ $(1 < n < 20)$ multilayer structures, Hebard *et al.* [273] showed that up to six electrons per C_{60} can be transferred from the Al to the C_{60} surface layer.

- McNally *et al.* [274] observed electric field-induced diffusion of Al into the bulk of C_{60} when studying thin-film Al-C_{60}-Al trilayer structures. According to their report the diffusion occurs very rapidly at field strengths on the order of 3.5×10^4 V/cm, which is considerably below the expected C_{60} dielectric breakdown field of $\sim10^6$ V/cm. Indeed, no structural breakdown of the C_{60} layer has been observed in this study [274].

- Most recently, Owens *et al.* [275] used photo-electron spectroscopy (PES) to study the electronic properties and morphologies of aluminum-C_{60} interfaces. They reported the formation of an interface dipole between the first layer of C_{60} and the Al surface, reflecting the transfer of approximately 0.2 electrons per first-layer fullerene. Deposition of Al onto C_{60} at 300 K resulted in formation of Al clusters on the surface and also in limited Al diffusion into the fullerene lattice. These interstitial Al atoms are believed to create a solid solution and to form donor levels that are thermally ionized [275]. Aluminum overlayer growth at 60 K results in smaller islands and suppressed doping because both surface and bulk diffusion are thermally-activated processes. Owens *et al.* [275] found no evidence of bulk Al-C_{60} compound formation, however.

In all cases, the nature of the fullerene-surface interaction is attributed to an electron charge transfer mechanism from the metal surface to the fullerenes. One would then expect that other metals should interact with the fullerene surface layer in a manner similar to that of aluminum. Indeed, many published reports corroborate this conclusion:

- A number of Scanning Tunneling Microscopy (STM) results show that C_{60} interacts strongly with metal surfaces, such as Al [272], Cu (111) [276], Ag (111) [277], Au (111) [278], Au (001) and Au (100) [279]. The interaction with these metal surfaces is much stronger than the C_{60}–C_{60} interaction.

- Surface-enhanced Raman scattering (SERS) provides yet another informative probe of the interaction between fullerenes and substrates. For a monolayer of C_{60} on noble metal substrates, downshifts in the Raman-active mode frequencies were generally observed, with some modes downshifting more than others. Using the strong Raman $A_g(2)$ pentagonal pinch mode as a calibration standard, downshifts between 15–18 cm^{-1} were observed on Au surfaces, between 26–28 cm^{-1} on Ag surfaces, and 23 cm^{-1} on Cu surfaces, indicative of the increasing interaction between C_{60} and the Au, Cu, and Ag surfaces in that order, and consistent with the sequence of work functions for the substrates Ag (4.3 eV), Cu (4.7 eV), and Au (5.1 eV) [280].

- Sarkar and Halas [281] have demonstrated a pronounced diffusion of silver (Ag) atoms into C_{60} thin films. The diffusion process was observed to be significant at temperatures just above room temperature, with an activation energy of 2.5 ± 0.5 eV. Temperature-dependent conductivity measurements indicate [281] that silver atoms form an impurity band in solid C_{60} with an activation energy of 0.26 eV.

- We have also found that C_{60} trilayers structures with gold electrodes (Au-C_{60}-Au) always yield samples that appear to be shorted, with measured resistance values on the order of Ohms. (This result has been corroborated by reports from other groups [282, 283].) This suggests that gold is penetrating into the bulk of C_{60} (perhaps, by forming pinholes, rather than by diffusion).

In general, the bonding of fullerenes to some substrates is strong while to others it is weak. Furthermore, metals tend to have a lower work function than semiconductors. Because of the band gap between the occupied valence band and the empty conduction band in semiconductors, more energy is usually required to remove an electron from its highest-lying occupied state to the vacuum level, as compared to a metal. Thus it is expected that charge is more easily transferred between a fullerene and the substrate in the case of a metal. Consequently, fullerenes should bind more strongly to metal surfaces than to semiconductor or insulating surfaces [23]. This argument is in general applicable to real C_{60} interfaces with substrates, except in cases where the semiconductor has a high density of surface bonds, such as the Si (111) and Si (100) surfaces. The binding of C_{60} to oxides such as SiO_2 and sapphire (α-Al_2O_3) is weak, while the binding to metals such as Al, Au, Ag, and Cu is strong [23].

Having established that a dipole moment due to a C_{60}/metal interface resulting in additional polarization is possible, we must still explain how it accounts for the dynamics of the dielectric loss peak that we observe. Recalling that the loss peak develops and then decays with oxygen exposure, we must rule out the possibility of a mere interfacial polarization, for such polarization would simply add a constant to the permittivity, without affecting dielectric loss at all. However, if we allow for the possibility of diffusion of metal atoms from the electrodes into the bulk of C_{60} (as indicated by some of the studies outlined above), then a charge transfer mechanism similar to that developed for oxygen diffusion (Sec. 4.7.3) would apply, resulting in frequency-dependent polarization and a dielectric loss peak at low frequencies. One might then account for the peak's dynamics (similar to that described in Sec. 4.7.4) by proposing that, as metal (*e.g.*, Al) atoms oxidize, they become less mobile, which prevents them from hopping between adjacent C_{60} interstitials, thereby eliminating dielectric dispersion.

While not impossible, this mechanism appears rather far-fetched. However, further controlled experiments are necessary to fully discount this possibility.[14] In the next Section, we shall concentrate on the oxygen-based mechanism developed in Sec. 4.7.2–4.7.5.

[14] It should be noted, however, that all of our reasoning would apply to the interfacial metal diffusion-induced polarization in exactly the same way that it applies to the oxygen diffusion-induced effect.

4.8 Temperature dependence of the dielectric function in oxygenated C_{60}

4.8.1 Dielectric behavior at $T > T_{01}$

The preceding discussion indicates rather strongly that the long range transport related to chemical diffusion and the reorientation of the induced dipoles due to tracer diffusion are two aspects of the same physical process. Since most of the electron charge carriers in oxygenated C_{60} are trapped, and thus not available for conduction (as evidenced by variations in conductivity of C_{60} by as much as ten orders of magnitude as a function of oxygenation — see, *e.g.*, Table 4.1), it is possible that ionic conduction due to oxygen diffusion contributes significantly to the DC conduction in oxygenated C_{60}. This would suggest that the magnitude of the activation energy of the peak dielectric loss frequency E_τ related to dielectric relaxation due to oxygen hopping is close to the magnitude of the activation energy of the DC conductivity E_σ, which we have measured to be $\sim$0.5 eV (see Sec. 4.4.2).

To test this hypothesis, we measured the dielectric properties of C_{60} films (0.1Hz$<$ f $<$100kHz) versus temperature (100K$<$ T $<$300K). The results of this study are presented in Fig. 4-25. The highest-frequency dielectric loss peak in Fig. 4-25(b) corresponds to 290 K, and the loss peak moves down in frequency, as the temperature is lowered in steps of 5 K to 215 K. As demonstrated in Sec. 4.7.2, the peaks that we observe are not Debye-like, as evidenced by the higher-frequency slope of $1-n=0.7$ (on the log scale) in the dielectric loss peak [Fig. 4-25(b)]. This indicates that our system is somewhat correlated [177] [a slope of unity ($n=0$) in the Debye loss peaks corresponds to uncorrelated systems], so that an oxygen molecule hopping from one interstitial site to the next is likely to increase the hopping probability of a neighboring oxygen molecule (see Fig. 2-19 and accompanying discussion in Sec. 2.3.3). This is consistent with our observation that, as a greater fraction of the interstitial sites gets

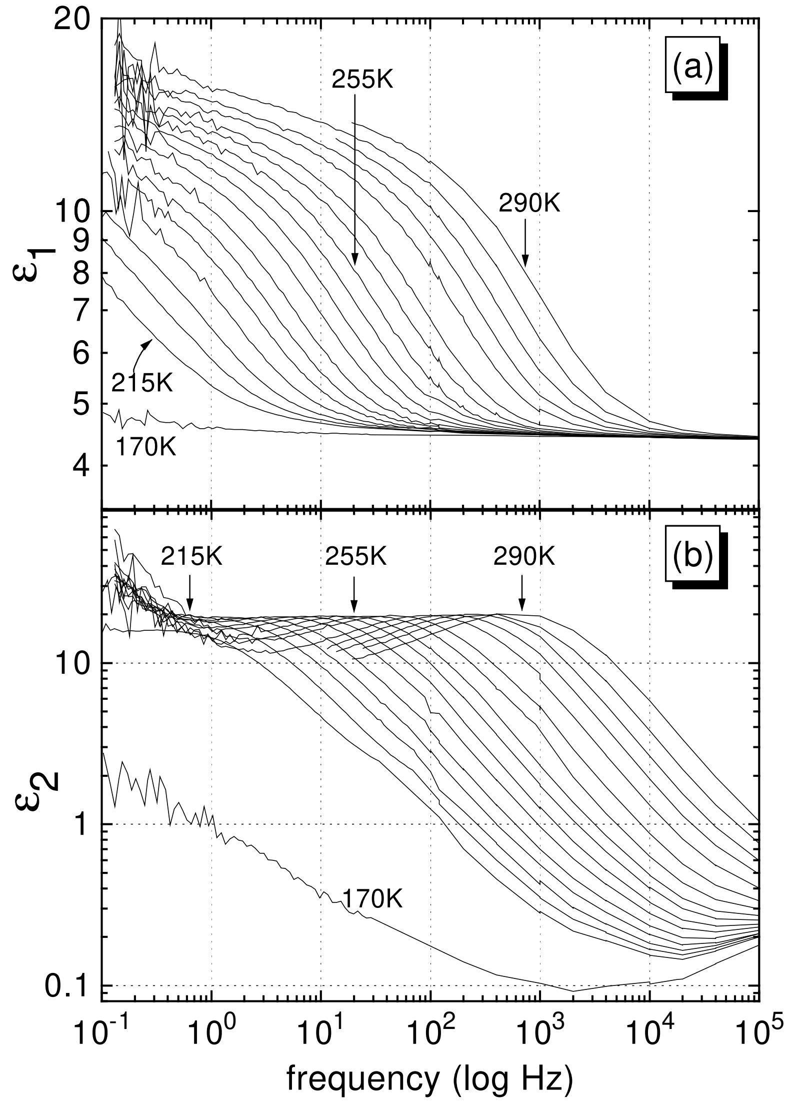

Figure 4-25: Frequency dependence of the real (a) and imaginary (b) parts of the dielectric function of a 840 Å-thick C_{60} film plotted on the log-log scale for temperatures 215–290 K in 5 K intervals. The loss (ε'') peak is activated with a $E_a = 0.5$ eV energy barrier and a frequency prefactor of 2×10^{12} Hz (as found from the Arrhenius plot in Fig. 4-26). The loss peak in the ε'' vs ω plot is not Debye-like, as evidenced by the higher-frequency slope of −0.7 (on the log scale), indicative of a correlated system. The broad increase in the loss function beyond 100 kHz for the low temperature $\varepsilon''(\omega)$ traces is due to residual rotations of C_{60} molecule below the $T_{01} \approx 260$ K structural "freeze-out" transition. The hopping of the oxygen molecules also freezes out below ~190 K, resulting in a decrease of the slope of the dielectric loss (ε'') and in a leveling off of the polarization (ε') [see also Sec. 4.8.2].

filled by the oxygen diffusion, the system becomes increasingly more correlated, until the loss peak disappears completely.

An Arrhenius plot of the frequency position of the dielectric loss peaks shown in Fig. 4-25 is plotted in Fig. 4-26. We find that the peaks are indeed temperature activated with

$$f = f_0 \exp\left(-\frac{E_a}{k_B T}\right), \tag{4.21}$$

where E_a is the activation energy, and f_0 is the frequency prefactor. From Fig. 4-26 we find that the activation energy of the loss peak below the phase transition at $T_{01} = 260$ K is 0.35 eV whereas the activation energy above the phase transition is 0.49 eV, with a frequency prefactor $f_0 = 2 \times 10^{12}$ Hz comparable to the phonon frequencies. Comparing the high temperature ($T > T_{01}$) activation energy of the peak frequency E_τ to the activation energy of the DC conductivity E_σ of our C_{60} films (Fig. 4-6 in Sec. 4.4.2), we find that the two are about the same and equal to $\sim$0.5 eV. This result has been confirmed for several samples of various geometries, but we are not yet completely convinced that $E_\tau = E_\sigma$ holds universally for this system. More experiments are needed to confirm this point. If this relationship holds in subsequent investigations, it will add much credibility to our hypothesis linking oxygen ions to the long-range charge transport in C_{60} films.

Since the suggestion that the activation energy of the DC conductivity of the film E_σ may be the same as the activation energy of the dielectric loss peak E_τ is one of the more intriguing results of our study, it is worthwhile to review the literature for other examples and theories where the same has been shown to be the case.

There are two basic kinds of theories that have been use to explain this behavior. In the first, the separate ionic hopping events are independent and have a broad distribution of relaxation times, while in the second, collective effects occur so that each hopping ion has strong interactions (usually of the Coulombic type) with surrounding ions. These two types of mechanisms have been called *parallel* and *series* conduction processes, respectively, by Elliott [284].

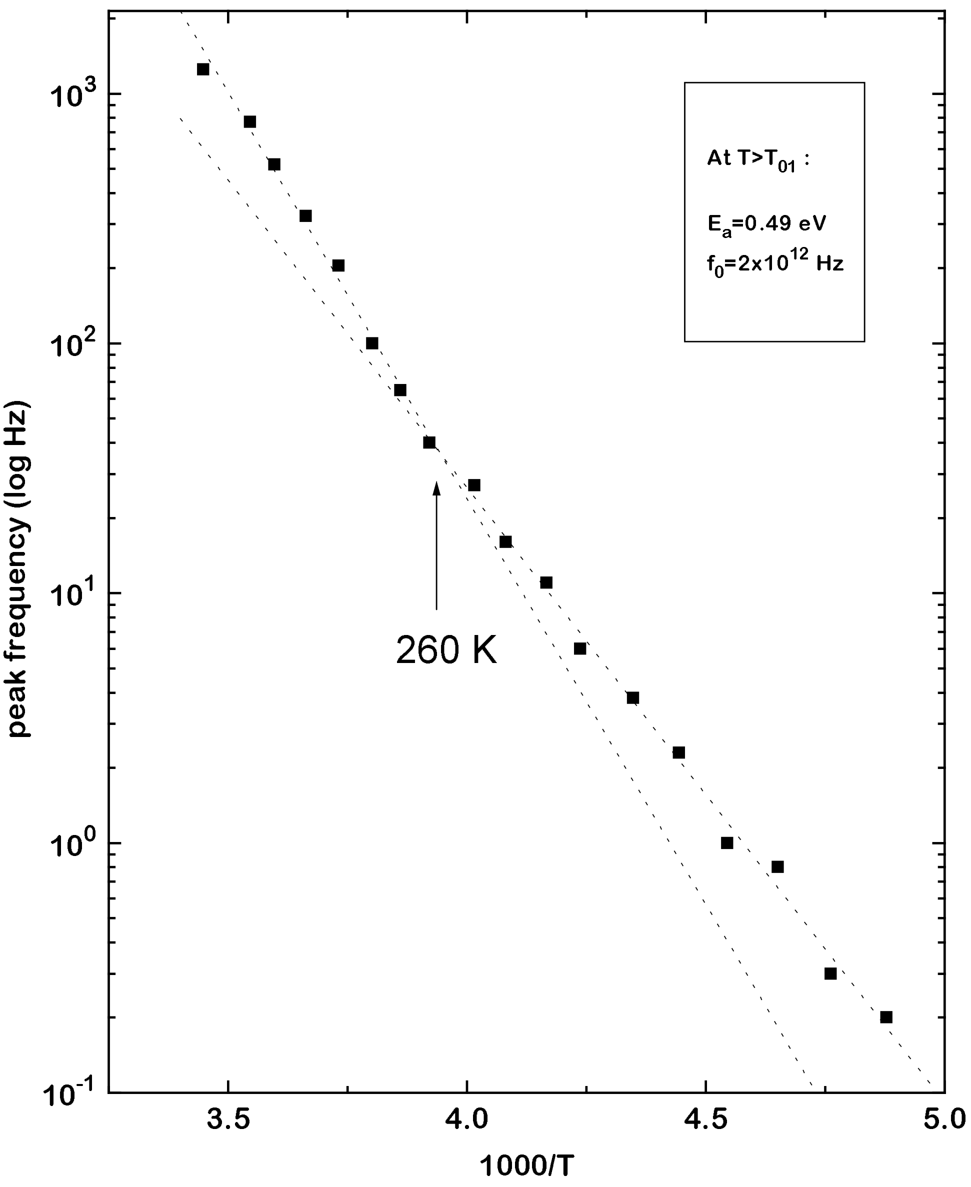

Figure 4-26: Arrhenius plot of the position of the (tracer) dielectric loss peak frequency shown in Fig. 4-25.

The series-type theories have received considerable attention recently, and they appear to explain the $E_\sigma = E_\tau$ effect rather well. In the macroscopic approach by Ngai *et al.* [285–288], called the "coupling model," the cooperative adjustment of the environment of the migrating ions leads to a stretching out of the relaxation process to times much larger than the primitive relaxation time for a non-interactive jump. Here it is implicitly assumed that the DC conductivity and AC relaxation are coupled (derived from the same underlying process).

In a more microscopic theory, called the "jump relaxation model," Funke [289–291] points out that the influence of a "cage effect potential" due to surrounding ions can lead to a high probability of return of the jumping ion ("unsuccessful jump"), which contributes to the AC relaxation, and not to the DC conductivity. This theory can explain why $E_\sigma = E_\tau$ by the fact that both successful and unsuccessful jumps involve the same potential barrier. It would seem, however, that this statement would be valid only for strong electrolytes, since it is difficult to see how E_τ can include an energy that determines the increase in the number of carriers with increasing temperature in this model.

Still another theory of the *series* type is the "diffusion-controlled relaxation" model of Elliott [284], which incorporates cooperative ionic motions, and has some formal similarity to Funke's model. This model, too, predicts that $E_\sigma = E_\tau$ only for strong electrolyte materials.

In all of these theories, the important point is that the AC relaxation process and the DC conductivity are both parts of the same process of interactive ion jumping. In the O_2/C_{60} system considered in our study, this would imply that oxygen diffusion through the C_{60} lattice contributes substantially to the DC conduction process in C_{60}. Since electrons in oxygenated C_{60} are trapped by the deep trap states, and are largely unavailable for DC conduction (as evidenced by extremely low conductivity of oxygenated C_{60} — see Table 4.1 in Sec. 4.4.2), we should consider this proposition increasingly plausible.

We briefly mention an alternative approach that involves a model of hopping conductivity [292]. This approach was originally developed to explain electronic conduction in disordered systems, but it is also applicable to ionic hopping processes. In it, the AC hopping conductivity is described by an equivalent circuit consisting of a random-resistor network with capacitors. At high frequencies, the jumps occur only between nearest sites, corresponding to an AC response that is mostly capacitive. At lower frequencies, multiple hopping can be described in terms of more highly conducting regions (clusters) surrounded by regions of poorer conductivity. Finally, as $\omega \to 0$, all capacitor-related impedances become infinite, and the conductivity is controlled by an infinite critical cluster of resistors. An analogous model was developed by Efros and Shklovskii [293] and by Balagurov [294] to describe the conductivity of a system consisting of randomly distributed metallic particles in a dielectric matrix near the percolation threshold. Another prominent theory of this kind, developed for ionic conducting glass systems, results in the Barton [295]-Nakajima [296]-Namikawa [297] (BNN) relation, which links the DC (static) dielectric constant $\varepsilon'(0)$ to the DC conductivity σ_{DC} as

$$\varepsilon'(0) \propto \frac{\sigma_{\mathrm{DC}}}{\omega_t}, \tag{4.22}$$

where ω_t is the frequency of the (tracer) dielectric loss peak. The BNN model has recently been popularized by Hunt [298–305]. If $\varepsilon'(0)$ is independent of T (as it seems to be in the case of C_{60}), then Eqn. (4.22) requires that both ω_t and σ_{DC} have the same temperature dependence. This model, therefore, also predicts $E_\sigma = E_\tau$, and it has an added benefit of not being limited to strong electrolytes, as is the case for some of the other theories.

4.8.2 Dielectric behavior at $T < T_{01}$

Let us now return to Fig. 4-25 and consider the dielectric behavior of our system below the C_{60} structural transition.

At temperatures below the $T_{01} \approx 260$ K transition, the C_{60} molecules are not free to rotate any more (see Sec. 1.3.2) and the losses associated with their rotational motion ($\omega_{rot} \sim 10^9$ Hz at $T \sim 300$ K [73]) are moving into our frequency range ($\omega_{rot} \sim 10^5 - 10^6$ Hz at $T \sim 160$ K [52, 72]) and appear as a broad increase in the loss function above 100 kHz. Below ~190 K the absolute value of the slope of the dielectric loss curve is starting to decrease as well, reaching $n - 1 = 0.37$ at 170 K [the bottom curve on Fig. 4-25(b)]. This shows that at low temperatures the hopping motion of the oxygen molecules freezes out, and the system becomes more strongly correlated, which, in turn, results in a leveling off of the polarization [see the bottom curve on Fig. 4-25(a) corresponding to the frequency response at 170 K].

An argument can be made that the decrease in the $n - 1$ exponent below 190 K is the result of the second-order phase transition in C_{60}, which is frequency dependent. The results of measurements of T_{02} by various methods at different frequencies are presented in Fig. 4-27 [306]. Following the linear dependency demonstrated in Fig. 4-27, and given that 100 kHz is the highest frequency we can access, we can expect the onset of the second order transition at $T \approx 200$ K, which is precisely what we observed in Fig. 4-25.

Additionally, in Fig. 4-28 we plot the capacitance C and loss tangent D of a 655 Å-thick C_{60} film versus temperature at 100 kHz. We recall that, at 100 kHz, no additional polarization due to oxygen occurs, and all of the dielectric properties measured are those of intrinsic C_{60}. A large anomaly, with an onset at ~ 230 K and reaching maximum at ~ 190 K, is clearly seen in the capacitance plot in Fig. 4-28(a). It is likely that this anomaly is indicative of the second-order phase transition, and is associated with the frozen-in orientational disorder [69, 76]. It can be inferred from Fig. 4-28 that the ratcheting motion of the C_{60} molecules responsible for the increased polarization decreases for temperatures from ~190 K down to ~65 K, and dies down completely for $T < 65$ K, as discussed in Sec. 1.3.2.

For comparison, we also show in Fig. 4-29 the data for the real and imaginary

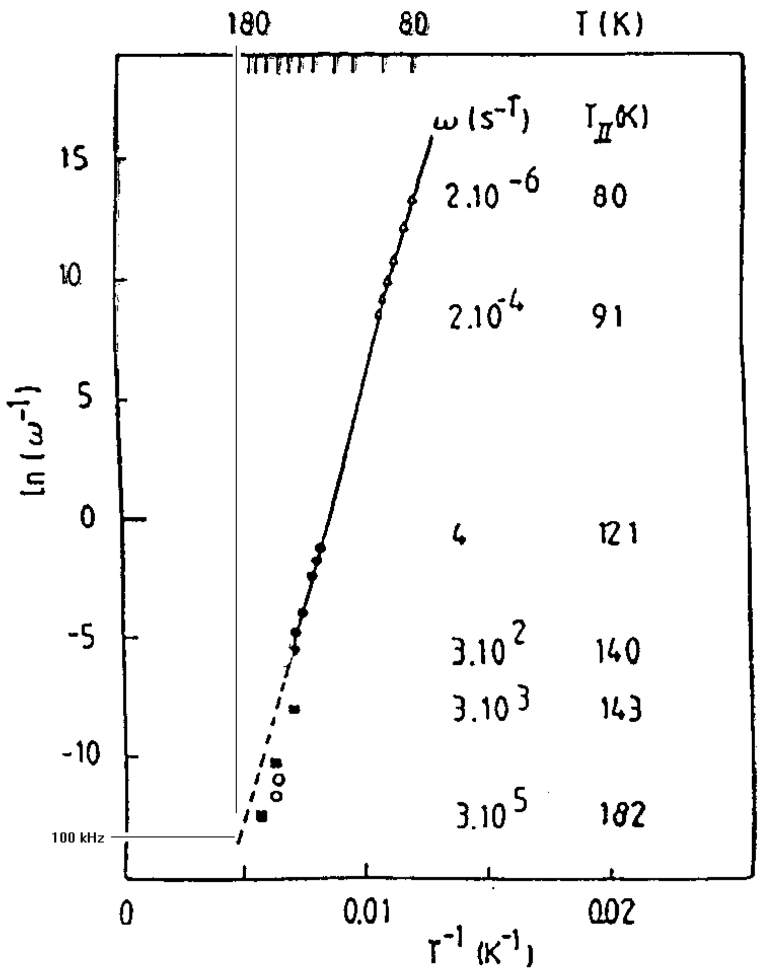

Figure 4-27: Plot of $\ln(\omega^{-1})$ vs T^{-1} for different measurement frequencies. The points, triangles, full squares, and open circles are taken from elastic constant [306], thermal expansion [307], dielectric [76], and sound velocity [52], measurements, respectively. The T_{02} values for each frequency are listed [306].

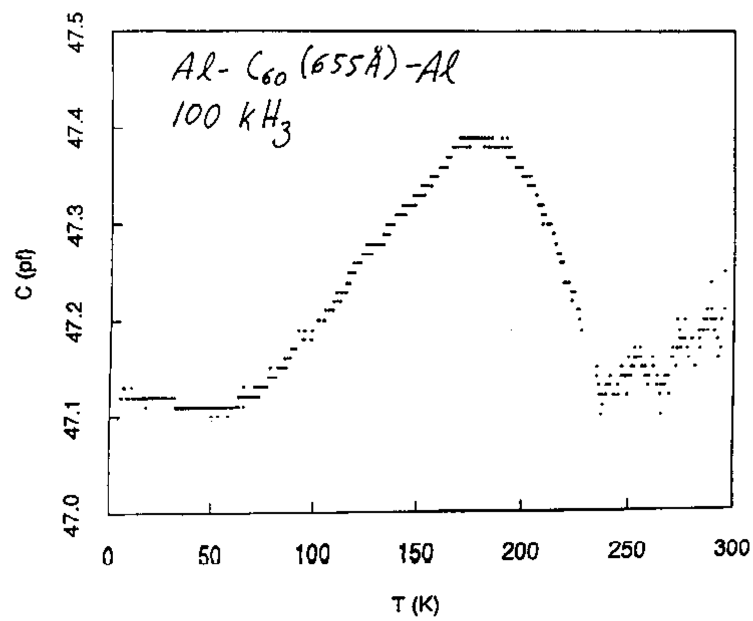

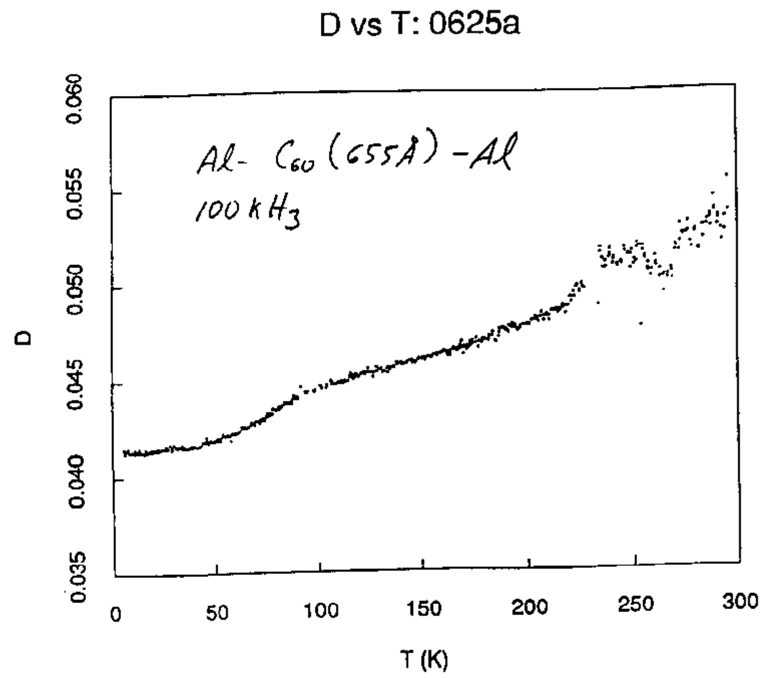

Figure 4-28: Capacitance (a) and dielectric loss tangent (b) vs temperature, for a 655 Å-thick C_{60} film. The measurement was conducted at 100 kHz to avoid the effect of oxygen and other impurities.

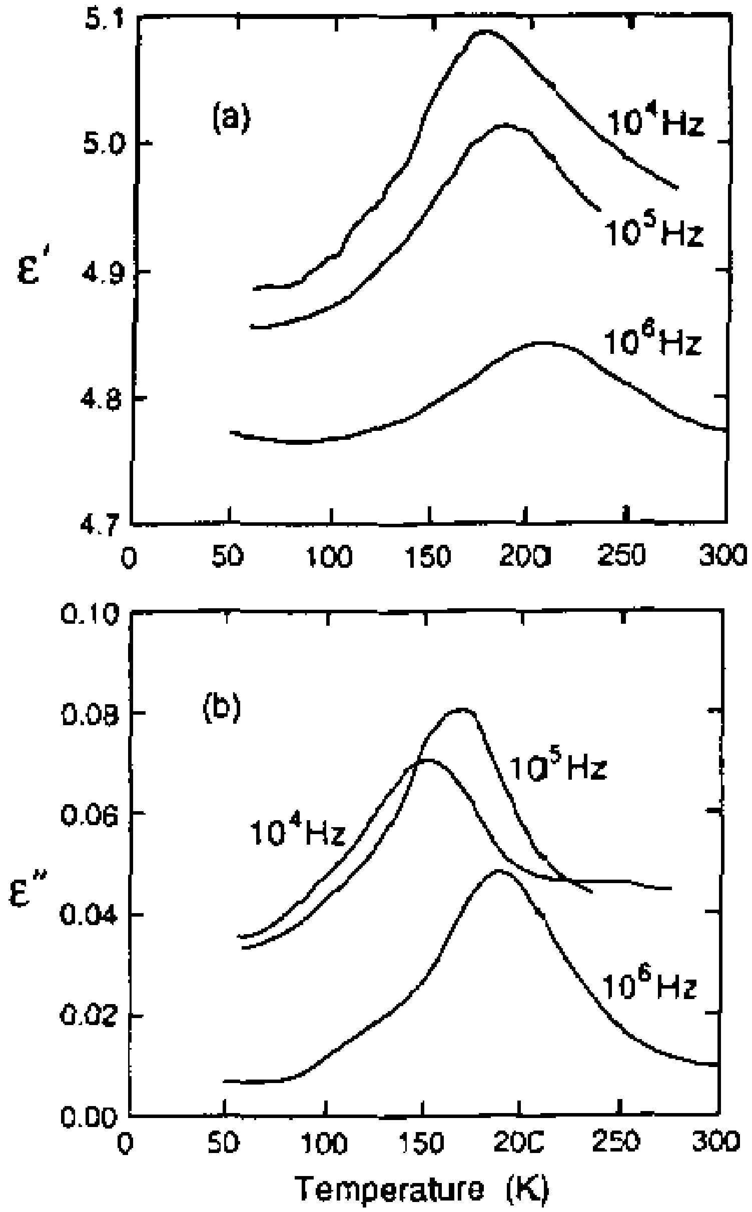

Figure 4-29: Real (a) and imaginary (b) parts of the dielectric function of a C_{60}/C_{70} mixture pellet plotted as a function of temperature at different frequencies [308].

parts of the dielectric constant of C_{60} plotted as a function of temperature at different frequencies that has recently been reported by Chern *et al.* [308]. We can see that the position of the peak in the 10^5 Hz trace for $\varepsilon'(T)$ in Fig. 4-29(a) agrees very well with our capacitance data reported in Fig. 4-28(a). The agreement in the dielectric loss data is less apparent, however, perhaps due to the fact that Chern *et al.* [308] present the imaginary part of the dielectric function $\varepsilon''(T)$ in Fig. 4-29(b), while we plot the dielectric loss tangent $D(T)$ in Fig. 4-28(b). Note also that Chern *et al.* [308] used a C_{60}/C_{70} mixture pellet in their work, rather than a pure C_{60} thin film that was utilized in our experiments.

4.9 Effect of humidity

As mentioned before, interstitial spaces in the weakly bound van der Waals lattice of the C_{60} solid are large enough to accommodate any of the chemical elements, and many of the smaller molecules (*e.g.*, molecular oxygen). We have verified that nitrogen gas (N_2) does not affect the dielectric and transport properties of fullerites, and this is consistent with evidence obtained from the NMR experiments [244, 252]. The other molecular species present in the ambient environment is water (H_2O), whose concentration can be measured in terms of the humidity of the environment.

There are a number of reasons why water molecules are an extremely unlikely source for the polarization increases in C_{60} films that we observe at low frequencies:

1. None of the sample characterization techniques reported in Sec. 4.5 (including the highly accurate infrared probe) were able to detect any amount of water present in our samples after days of storage in an ambient environment with variable humidity.

2. Hamza *et al.* [272] found that multilayer and monolayer coverages of C_{60} on aluminum passivated the surface such that exposure of the surface to water at room temperature led to no oxidation of the surface. This suggests very strongly

that water does not penetrate a polycrystalline C_{60} film in any way — either along the grain boundaries or via diffusion into the interstitial spaces.

3. While the permittivity of water ($\varepsilon' \approx 78.5$ at $T = 300$ K [309]) is certainly high enough to affect the permittivity of the host material that water diffuses into, this increase in permittivity (as usual, accompanied by a loss peak in ε'') would occur at gigahertz frequencies[15], rather than at $\sim 100 - 1000$ Hz frequencies, as is the case in our experiments.

Taken together, these arguments rule out the importance of water as the source for an increase in permittivity and the associated dielectric loss peak in C_{60} at low frequencies. If anything, the presence of water might be responsible for the small discrepancy[16] between the $\varepsilon' = 3.9$ value for permittivity of C_{60} observed in optical experiments [61] and the $\varepsilon' = 4.4$ value observed at 100 kHz [24].

While not participating in dielectric relaxation, water, when accumulated on the surface of the measured film, can increase the conductivity of the film, affecting the measured dielectric properties at low frequencies, as described in Sec. 2.3.4. While a sample in the "sandwich" configuration (Fig. 4-13) does not have an open surface for water condensation, a sample prepared on a microdielectric sensor (Figs. 3-6 and 3-10) does, and dielectric properties measured with dielectrometry can, therefore, be affected by ambient humidity, as demonstrated below.

A microdielectric sensor with 1 μm inter-electrode spacing and 1 m meander length (see Fig. 3-10) was used for this experiment. After the deposition of a 1.88 μm-thick

[15]The large losses in water-containing materials at gigahertz frequencies (corresponding to the onset of the dipole-flipping process, as described in Sec. 2.3) are, in fact, utilized in such diverse applications as food cooking (microwave ovens) and geological surveying (which relies on variations in water content — and, thus, the dielectric constant — of different kinds of soils to map out the geological profile of the land without digging.)

[16]As was mentioned in Sec. 4.6, the other — and considerably more likely — possible reason for this discrepancy is losses associated with rotational motion that C_{60} molecules experience at $T > T_{01}$, reported to center at frequencies on the order of 100 MHz [52,73]. Surface Acoustic Wave (SAW) experiments in this frequency range should be able to quantitatively ascertain the losses associated with this rotational motion. Preparations for such a study, to be conducted in cooperation with a Raytheon, Inc. research facility, are currently under way.

C_{60} film onto the surface of the sensor, the device was taken out in the air, and the dielectric function of the C_{60} was measured as a function of oxygen diffusion using the Eumetric® System II Microdielectrometer apparatus (Micromet Instruments, Newton, MA), as described in Sec. 3.3.

In Fig. 4-30, we show the evolution of the dielectric properties of the film as a function of exposure to the ambient environment at room temperature. The uppermost dotted line represents the measurement taken within the first minute of exposure. Clearly, in an oxygen-free C_{60} sample, the static dielectric constant is dominated by conduction, since the conductivity of oxygen-free C_{60} films at room temperature is $\sim 10^{-6}$ S·cm^{-1} or less (see Table 4.1). However, in polycrystalline films, oxygen rapidly diffuses into the grain boundaries isolating C_{60} grains (crystallites) one from another and thus quenching the conductivity, reducing it by as much as seven orders of magnitude [257, 260] within a few hours of exposure. (A similar rapid quenching of the photoconductivity by oxygen in C_{60} films has been reported by Minami [310], Asakawa [262], and many others). The increased resistivity due to oxygen causes both the polarization and dielectric loss (decaying dotted curves in Fig. 4-30) to decrease dramatically within 13 hours [see inset to the Fig. 4-30(b)].

The big loss peak accompanied by a polarization increase re-appears again after 13 hours of exposure (solid lines in Fig. 4-30), signaling another increase in sample conduction. We have linked this effect to an increase in ambient relative humidity from $\sim$35% to $\sim$60%. With increased humidity, the moisture condenses on the surface of the sample, "shorting out" the electric field lines of the microdielectric sensor (Fig. 3-6(b)). This underscores the importance of making the sample thick enough (at least on the order of the inter-electrode spacing) when using the microdielectrometry technique.

As the humidity decreases back to its initial value ($\sim$35%) during the 28–45 hours of exposure [inset to Fig. 4-30(b)], the conduction-related loss decreases as well [dashed lines in Fig. 4-30(b,c)], and then disappears completely, leaving behind

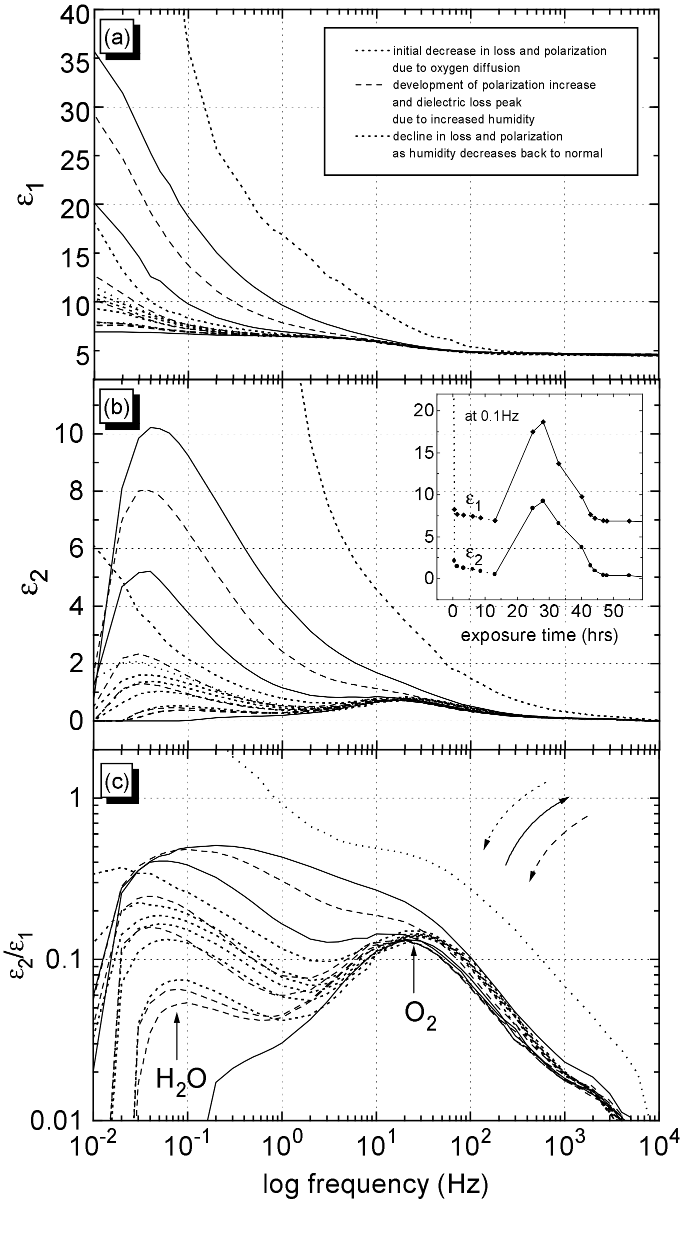

Figure 4-30: Frequency dependence of the real (a) and imaginary (b) parts of the dielectric function of a C_{60} polycrystalline film plotted on a log-linear scale, and the loss tangent (c) plotted on a log-log scale. Water (H_2O) and oxygen (O_2) related loss peaks are identified. The initial decrease in loss and polarization due to quenching of the conduction by inter-grain oxygen is shown by the dotted lines. The solid lines and the inset to plot (b) show the development, and dashed lines show the decay of the loss peak due to the surface moisture (see text). As the humidity decreases back to its initial value (~35%) during hours 28–45 of exposure (inset), the conduction-related loss decreases as well (dashed lines), and then disappears completely, leaving behind the Debye-like dielectric loss peak at ~30 Hz, corresponding to the lowest solid line.

the familiar dielectric loss peak at ~30 Hz due to interstitial oxygen hopping [the dashed line in Fig. 4-30(b,c)].

Note also that, regardless of the low frequency phenomena relating to water and oxygen effects, the relative permittivity ε' of C_{60} films measured with microdielectrometry at 10^5 Hz is in close agreement with $\varepsilon'(10^5\,\mathrm{Hz}) \approx 4.4$ determined from the capacitance measurements of $M/C_{60}/M$ (M=metal) trilayer structures (Sec. 4.6).

From the fact that the oxygen-related dielectric loss peak is not affected by humidity changes, we conclude that, as expected, water does not penetrate into the bulk of C_{60} lattice, but instead condenses on the surface of the film, resulting in large surface conductivity, which appears as a large low frequency loss peak in dielectric measurements (Fig. 4-30). This process is fully reversible and, as the ambient humidity decreases, so does the conductivity-related loss peak.

4.10 Effect of other film treatments

Keeping in mind that the original objective of this study was to produce a high-quality thin-film dielectric out of C_{60}, we have tried a variety of other film treatments, following the general philosophy for film modification outlined in Sec. 4.4. We briefly mention the results here, as they may be important in the future for technological reasons.

As demonstrated in Fig. 4-31, a ten-minute exposure of a ~1000 Å-thick C_{60} film to chlorine improved the film's dielectric properties considerably by both increasing the permittivity by ~15% and reducing the dielectric loss by as much as an order of magnitude. It is almost certain that, unlike oxygen, chlorine reacts with C_{60}, opening up C_{60}'s double bonds and attaching itself to the resulting free radicals [96]. Since the resulting compound appears to have intriguing dielectric properties, as evidenced by the data in Fig. 4-31, its chemical composition merits further investigations.

Similar improvements have been achieved by infusing nitric oxide (NO) into the

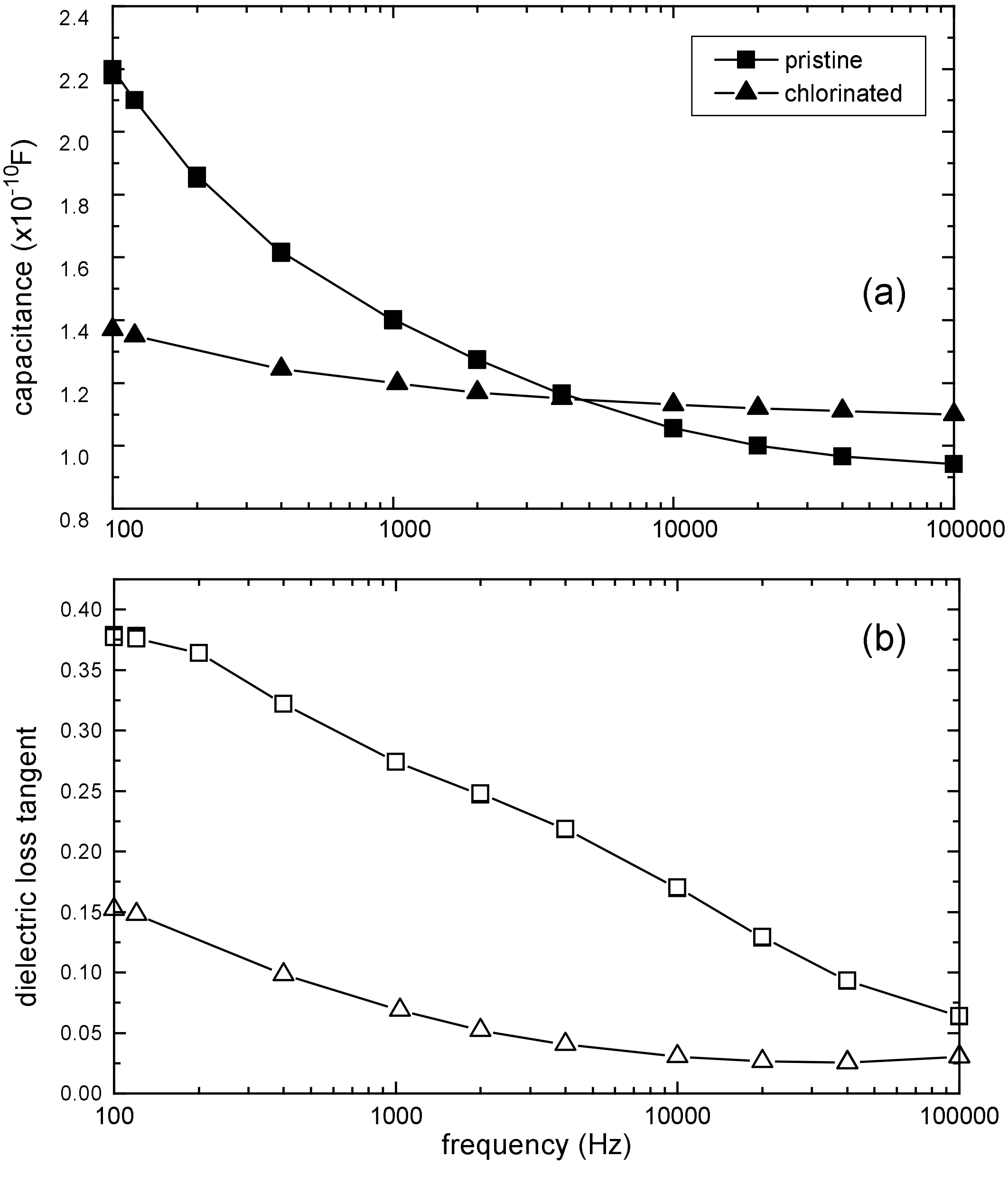

Figure 4-31: (a) Capacitance C and (b) dielectric loss tangent D vs frequency on a log scale showing the effect of 10-minute exposure of a 410 Å-thick C_{60} film to chlorine. A ~15% increase in permittivity and a large reduction in dielectric loss can be inferred from these data, indicating a significant improvement of dielectric properties of the C_{60} film.

C_{60} lattice.[17] By subjecting C_{60} crystalline powder to an NO environment at $T = 100°C$ and $p = 300$ psi for 4 hours, a film composition of $C_{60}(NO)_{0.88}$ has been achieved,[18] as determined by weight uptake measurements. Since NO is dipolar on its own, additional polarization due to NO simply adds to that of the C_{60} intrinsic polarization without introducing any additional loss mechanisms over the frequency range that we are dealing with. The result is a good low-loss dielectric less susceptible to oxygen-induced degradation (because most interstitials are already filled with NO). This achievement would have been of potential practical importance,[19] had it not been for the fact that NO is a highly toxic gas that is usually avoided in industrial environments.

In the two previous examples (Cl_2 and NO), we attempted introduce a "glue" or "filler" material into the interstitials of the fullerite that would make the solid more stable in the ambient environment, while at the same time enhancing its dielectric properties. A different way of achieving the same goal would be to attempt to "seal off" the interstitial spaces of the fullerene lattice by modifying the host material itself. As Fig. 4-32 demonstrates, we have achieved some success with reducing the dielectric loss of C_{60} films by growing them in the presence of UV light. While the physical reason for this effect is unclear, we hypothesize (and X-ray diffraction experiments confirm) that the improvement is due to the fact that the UV-grown films are more disordered (perhaps, cross-linked via photopolymerization, as described in Sec. 1.3.2), thus making it harder for oxygen or other impurities to diffuse into the bulk of the material and compromise its dielectric properties.

Another method to "seal off" the film is to cross-polymerize it, as described in Sec. 1.3.2. In Fig. 4-33, we compare the dielectric functions of pristine and pho-

[17] Using IR spectroscopy, Fastow *et al.* [311] have studied NO adsorption on C_{60} and demostrated that NO interacts relatively strongly with C_{60}. Similarly, a strong interaction has been reported between C_{60} and adsorbed CO [311] and CO_2 [312].

[18] The $C_{60}(NO)_{0.88}$ composition corresponds to the highest NO content that has ever been obtained. More typically, C_{60}/NO composites with somewhat lower NO content are produced [313].

[19] See also Sec. 1.7.6 outlining the possible use of NO to enhance the photosensitivity of C_{60} as a

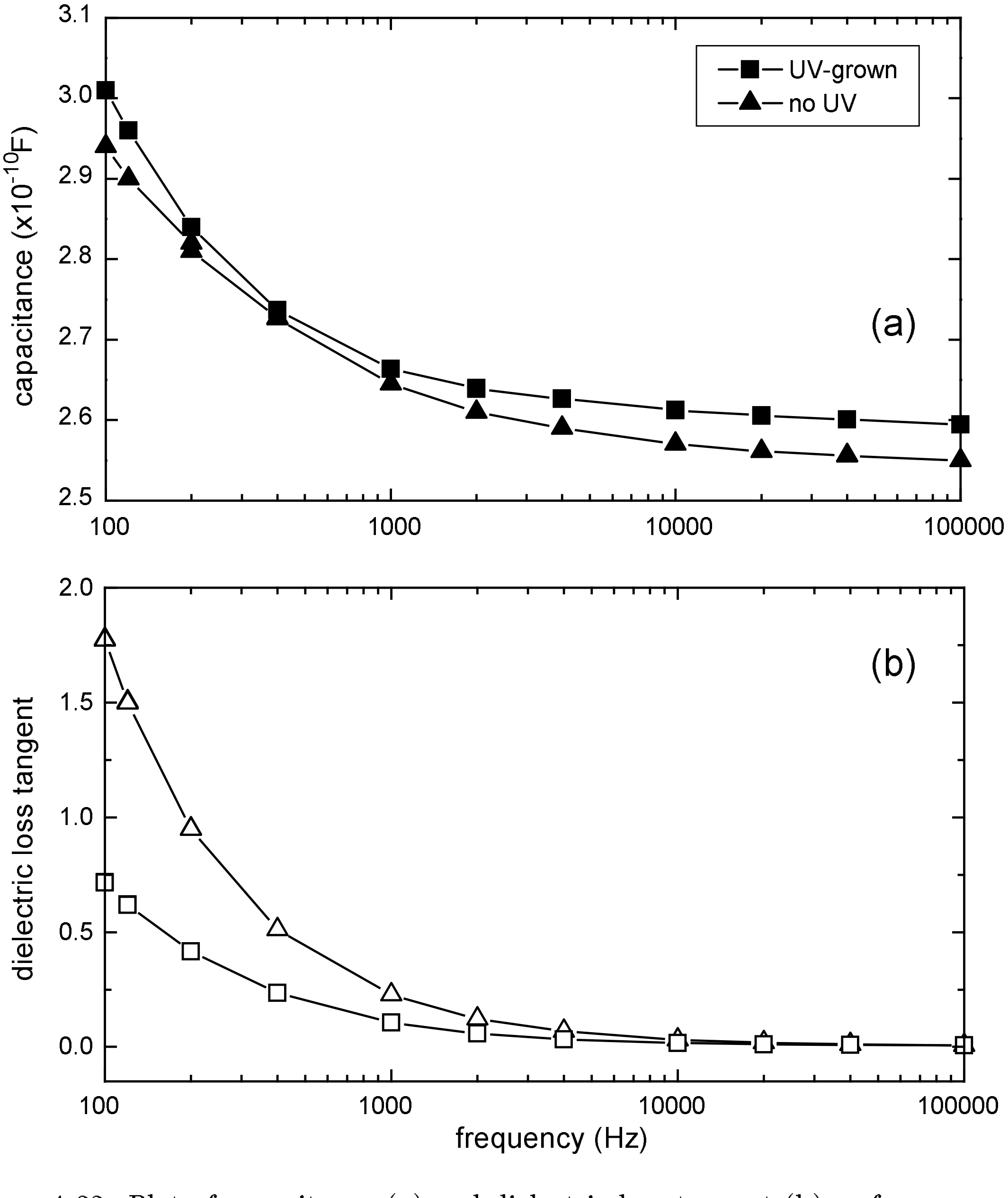

Figure 4-32: Plot of capacitance (a) and dielectric loss tangent (b) vs frequency (on the log scale) for C_{60} films of 1600 Å thickness grown in the absence (triangles) and in the presence (squares) of UV light during deposition. The data display evidence of lower dielectric loss at low frequency in UV-grown C_{60} films.

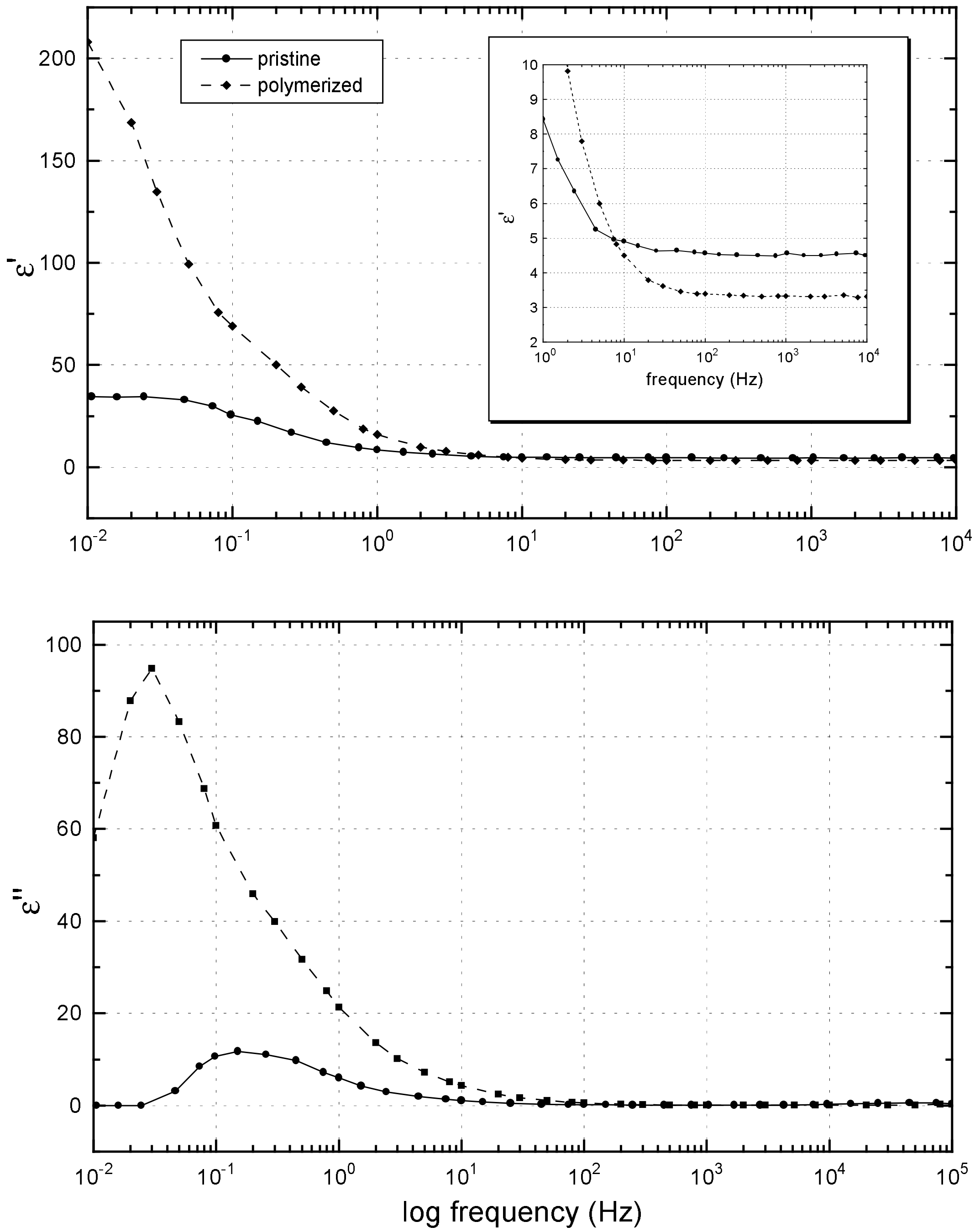

Figure 4-33: Real (ε') and imaginary (ε'') parts of the dielectric function of a 1191 Å C_{60} film before and after photopolymerization with a 488 nm Ar-ion laser source in vacuum for 10 hours at an average fluence of $1\,\mathrm{W/cm^2}$. The measurement was performed using the Micron sensor.

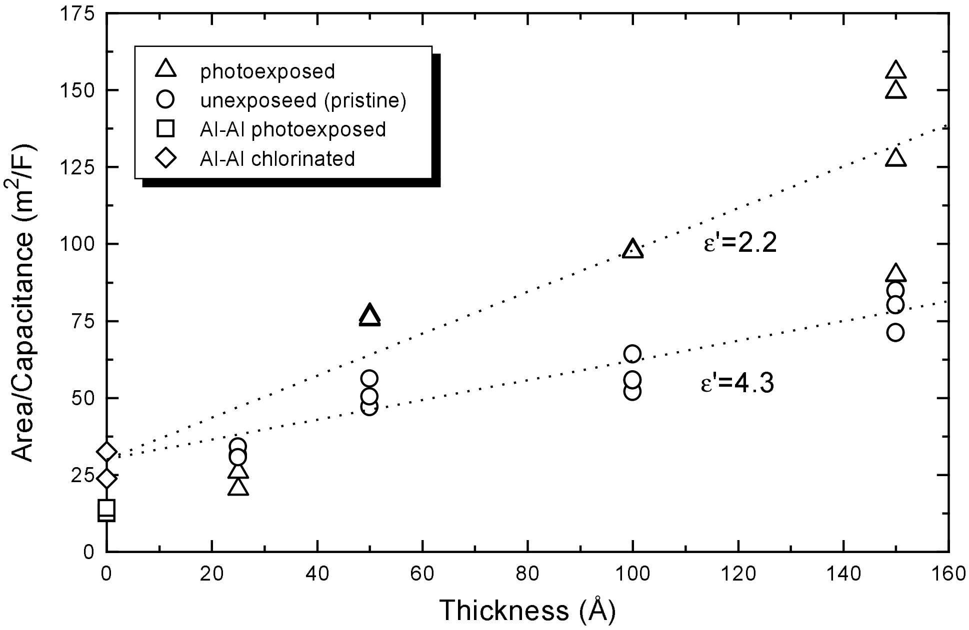

Figure 4-34: Plot of the reciprocal areal capacitance A/C vs thickness for pristine (circles) and UV-polymerized (triangles) C_{60} films demonstrating that UV-polymerization decreases the real part of the dielectric constant ε'. Control data points for photoexposed (squares) and chlorinated (diamonds) Al-Al_2O_3(ML)-Al junctions (without any C_{60}) are shown for reference.

topolymerized 1191 Å-thick C_{60} films measured with the Microdielectrometer. The most interesting finding, shown in the inset plot, is that the intrinsic dielectric constant of the polymerized C_{60} film ($\varepsilon' \approx 2.3$) is *lower* than that of the pristine C_{60} film ($\varepsilon' \approx 4.5$). This finding is consistent with the thickness dependence study presented in Fig. 4-34, in which we compare the dielectric constants of pristine and photoexposed fullerene films by showing a linear dependence of the inverse capacitance $1/C$ on thickness ℓ for each film.

photoresist in microelectronic fabrication applications [139].